ALTERNATIVE METHODS FOR MITIGATING NATURAL PHOTOVOLTAIC VARIABILITY: DYNAMIC HVAC LOAD COMPENSATION AND CURTAILED PV POWER

BY

JOHN ALEXANDER MAGERKO III

THESIS

Submitted in partial fulfillment of the requirements
for the degree of Master of Science in Electrical and Computer Engineering
in the Graduate College of the
University of Illinois at Urbana-Champaign, 2016

Urbana, Illinois

Adviser:

Professor Philip Krein

Abstract

Continued integration of renewable energy resources onto the electric grid increases variability and decreases grid stability. Energy storage can help mitigate some of these effects, but conventional energy storage such as batteries is typically expensive and has other disadvantages such as round trip inefficiency and limited lifetime. Real, high-speed solar panel data is used to characterize the stochastic energy output of PV sources, and the numerous challenges faced and methods used when manipulating this real-life data set are detailed. Two alternative methods are then presented to absorb or reduce the variability imposed upon the grid by PV or other generation. (1) Dynamic HVAC load compensation is shown to absorb or "filter" short-term PV variability and act as effective grid inertia. A proposed Butterworth filter power target technique balances energy storage demands with decreased uncertainty. A small-scale model of a variable speed blower and fan is used to provide a conversion between fan speed and power consumed and to estimate filtering limitations imposed by undesirable acoustic effects. Considering the acoustic, physical, and thermal limitations simultaneously, the variation absorption or filtering capability of dynamic HVAC load compensation is analyzed for various building sizes and on-site PV penetrations. The resulting reduction in battery storage capacity and utilization is briefly investigated. (2) PV operating reserve curtailment is introduced. The same Butterworth filter power set-point is used, its implementation is shown as feasible through simulation, and the variability reduction is quantified in two different ways. The claim is made that PV should be treated and priced like conventional grid generation, which is responsible for both energy and regulation capabilities. PV operating reserve curtailment is then shown to be economically favorable for at least *some* level of reserve. Finally, a proposed metric of optimality is presented that balances energy production with decreased variability.

Acknowledgments

To my ever-supportive family who has led by example and provided the encouragement and advice that enabled me to reach this milestone.

This work was primarily supported by the Grainger Center for Electric Machinery and Electromechanics at the University of Illinois with additional support from the Siebel Energy Institute.

Contents

1. Introduction and Motivation

Intermittent renewable energy resources are rapidly becoming significant players in the power generation landscape [1], but they have been shown to be extremely variable, even over short time scales of seconds to tens of seconds. Solar in particular can exhibit rapid power changes in the vicinity of 80% peak power on days where intermittent clouds block the sun. Figure 1.1 represents one such typical day with intermittent cloud cover. This unpredictability coupled with reduced traditional generation that solar is replacing threatens the stability and reliability of the electric grid [2]. The default solution to these challenges is typically energy storage in the form of batteries, but this thesis focuses on cheap, partial, alternative solutions that provide numerous benefits without the need for significant additional cost or hardware.

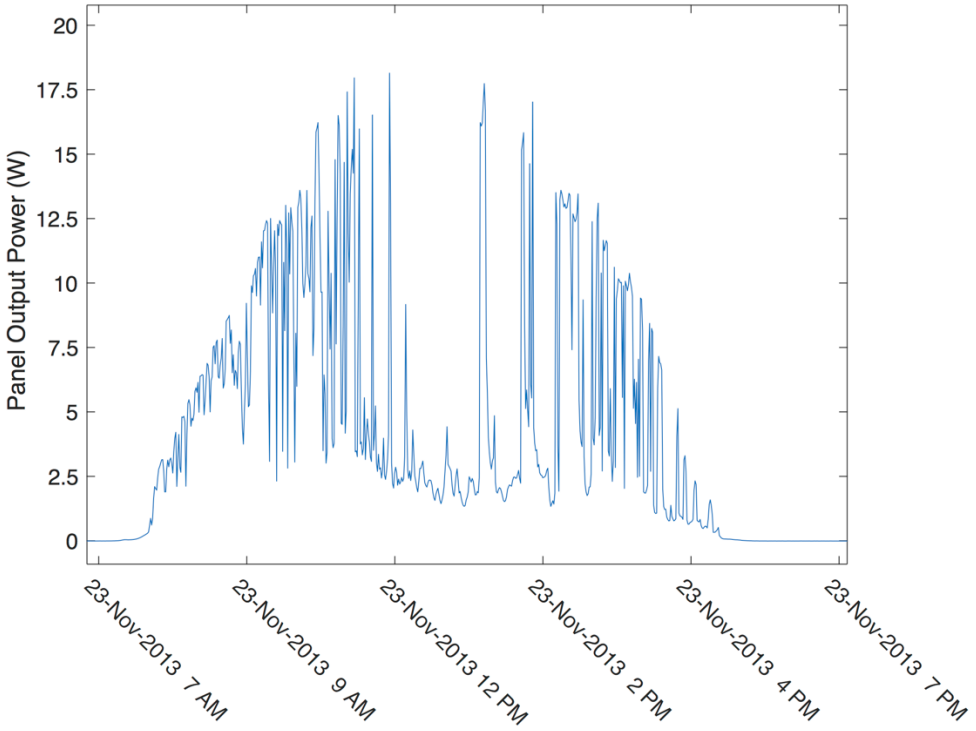

Figure 1.1. Sample power output from 20 W solar panel demonstrating rapid changes in PV power output.

1.1. Wind and solar as "negative loads"

The fundamental key to successful operation of the electric grid is maintaining power balance at all times. That means that at every instant in time power demanded must be met by power supplied. Thanks to a number of market structures and grid controls, small- to mid-size electricity consumers could turn on and off any electric load, unannounced, at any time, and the grid could maintain stable

operation. When wind and solar energy generation, specifically photovoltaics (PV), were introduced to the grid, they were treated in the same way as loads had been; independently owned wind and solar could produce largely unregulated amounts of power whenever it was available. Despite being electric generation units, neither wind nor solar were originally responsible for maintaining stability or reliability of the electric grid. In contrast, they were increasing variability and uncertainty. For this reason, these renewable resources were deemed "negative load" as they behaved just like typical electric loads might with the exception that they produced power rather than consumed it, and therefore utility companies could not charge them for the power flow or variation in power that they produced. Payment structures for electricity availability insurance or electricity prices for reverse flow are outside the scope of this thesis; however, the cost of variability imposed upon the grid is relevant. Arguably, as wind and solar become increasingly significant sources of energy and as their costs continue to fall, they, as generation sources, should be responsible for mitigating some, if not all, of their variability. The focus of this thesis is entirely on solar PV generation, though many of the same problems and potential solutions exist for wind or other resources as well.

1.2. Variability and inertia in the grid

Unless every generator and load schedules its future activities, temporary imbalances will be intrinsic to the grid, and this is normal; small load-change variations occur all the time, and the grid has operated satisfactorily with these and much larger disturbances (such as lightning, faults, or generator outages) for many decades. The key to grid stability is the inertia found mostly in large turbine generators. Any time a grid disturbance occurs, the rotational speed of the on-line generators changes, but their large inertia keeps them moving. This form of energy storage permits governors or other fast control mechanisms to maintain synchronous operation of generators and thus stability of the grid. Unfortunately, PV generators connect to the grid through power electronic inverters, and they do not possess any inherent inertia or significant energy storage; changes in irradiance on a solar panel translate to near instantaneous changes in electrical power output. On top of this, as PV produces more and more power, traditional generators will be taken off-line, further reducing the available stabilizing inertia on the grid and replacing predictable, controllable generation with hitherto stochastic sources. IEEE standard 1547 compounded all of these issues by requiring inverters to disconnect during faults, though such standards have been revised in recent years to allow for low-voltage ridethrough [3]. Nevertheless, the takeaway is that continued penetration of distributed PV systems is not sustainable unless the uncertainty and stability issues can be addressed.

1.3. Understanding and quantifying the problem

To address the issue of PV variability, it is important to identify the relevant time scales using long-term, real life solar data. No other random pattern generator can accurately simulate the stochasticity of real-life changes in irradiance, at least not until it is well understood. One of the major foci of this thesis is to quantify the variability at various time scales and ensure that all possible dynamics were captured and considered when performing this analysis. Previous work has differed in its definition of high-frequency solar data with sampling rates ranging from 1 min [4] to 20 s [5], [6] and topping out at about 1 Hz [7], [8]. As will be shown, all of these fall well short of the sampling frequency required to capture all possible fluctuations. Chapter 2 will detail the origins of the real-life data used and the assertion that the test setup captured all possible dynamics, discuss challenges encountered in using the raw data set, outline the procedures used to clean up the data set and make it useable, and present some results on what was deemed to be the magnitude of variation associated with various time scales.

1.4. Energy storage and proposed alternatives

After determining the extent of variability during the day, the question becomes how to mitigate it. In this thesis, the focus is largely on short-term diurnal storage as opposed to overnight, multi-day, or seasonal storage requirements (though thermal storage for such durations is possible, such as full-day energy storage with ice [9] or phase change materials [10]). To date, there are three main strategies for absorption or mitigation of PV induced grid variations with battery storage being the most common approach. The other two are generally called demand-side response and curtailed PV. Variations on these two latter strategies will be the focus of this thesis.

1.4.1. Traditional energy storage solutions

Traditional energy storage typically consists of a large bank of batteries (or supercapacitors) [11]–[13]. These units either connect to the PV string DC bus (Figure 1.2.a) or through a bidirectional converter to an ac circuit breaker or grid (Figure 1.2.b). There are some positive aspects of batteries as a variability reduction solution. The system can be highly modular and is therefore expandable and relatively easy to implement as a post-market solution. Unlike the alternative solutions that will be presented, batteries can also enable long-term energy storage in place of, or even in addition to, short-term variability reduction. Such capability highlights the cycling limitation associated with batteries, however. Batteries designed for long-term deep discharge are usually not also capable of short, high-power bursts without degrading the battery lifetime (the number of times it can be charged and discharged before requiring replacement). In addition, all battery storage solutions present possible chemical and fire hazards; they

also suffer from round-trip inefficiencies, i.e. energy losses associated with voltage conversion, Coulombic efficiencies, and other losses associated with charging and discharging. Perhaps the largest downside to battery storage is cost. Long-term goals of $150/kWh and $0.010/kWh/cycle ($10/MWh/cycle) of cycled energy have been discussed for storage [14]. In contrast, the two alternatives proposed here cost very little to implement and should be cheaper alternatives overall, even when taking into account the cost of energy losses. Other solutions such as supercapacitor banks or flywheels were not investigated, though they suffer from their own short-comings, primarily cost.

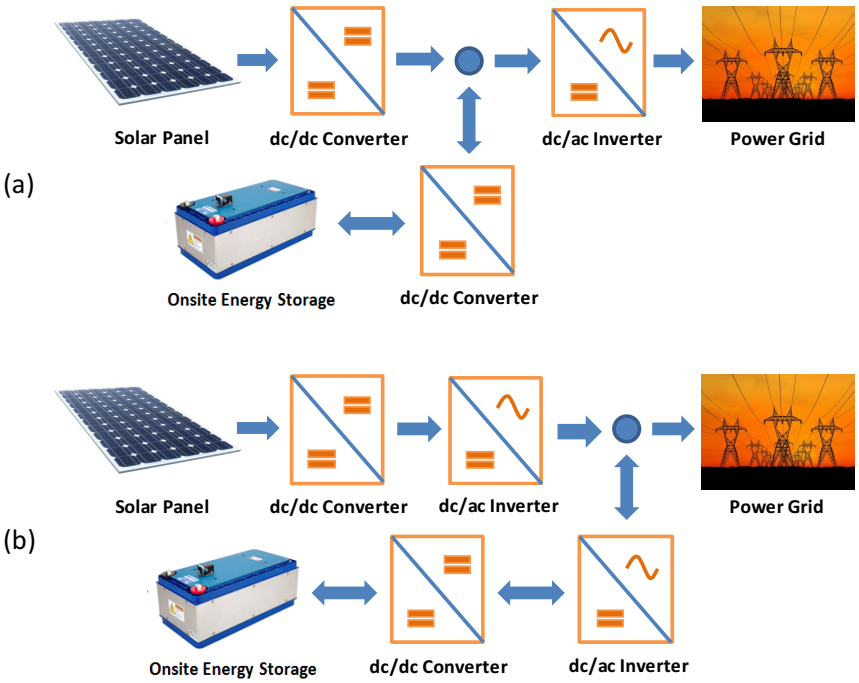

Figure 1.2. Energy flow for a PV system with battery storage where (a) the battery is connected to the dc bus and (b) the battery is connected through a bidirectional inverter onto the grid side.

1.4.2. Variable speed drives in HVAC

Energy-efficient buildings, including several net-zero energy commercial buildings, have been constructed around the globe. Research activities on this topic have increased in recent years [15]–[18], and many occupants have shown interest in having net-zero energy buildings as their future offices such as the new Apple "Spaceship" in Cupertino, California [19]. Energy efficient or net-zero energy buildings often include onsite photovoltaic (PV) solar panels that, as mentioned, provide non-constant power that can vary rapidly. Considering this inconstancy to represent an unwanted ac signal from a PV system, a suitable filter could be implemented but would require storage. If instead one utilizes the thermal storage capacity or thermal inertia inherent in a building, then HVAC (heating, ventilation, and air-conditioning) system adjustment can emulate electrical storage, much like an electric swing bus [20]–

[24]. To clarify, after converting electricity to thermal energy, the reverse would not take place as such conversion is inefficient. Instead, the "release" stage of this energy storage would be experienced when an HVAC system consumes less energy than it otherwise would to heat or cool the given space. Such an electric swing bus could offset fast variations of local solar power from a grid perspective with reduced need for conventional storage. The scaling potential is sizeable, given that nearly 40% of annual U.S. energy is consumed in residential and commercial buildings [25] with nearly half of that consumed by HVAC systems [26].

This thesis will demonstrate in Chapter 3 how intelligent control of HVAC drives can compensate, within predetermined frequency and amplitude limits, for onsite solar power over short time intervals without disrupting building temperature and comfort. The process is based on concepts in [20]–[22]. In particular, [20] shows how bandwidth concepts can take advantage of HVAC dynamic adjustment to offset energy resource variability. Power electronics enables this control via dc-dc converters, inverter-based drives, and other existing hardware, as illustrated in Figure 1.3. The results formally take advantage of thermal energy storage, but in this thesis the emphasis is on mitigating fast dynamic variability, more akin to treating HVAC as accessing thermal inertia. Utilizing thermal inertia can alleviate the need for inherently expensive, fast-varying, grid-side (or building-side) resources. This is nearly equivalent to placing a low-pass filter on a building's net generation and usage, requiring grid-side assistance only when changes in load-side demand persist beyond an extended interval [27]. Given the slow thermal response of a building, we might anticipate that time scales of a few minutes or faster can be used to advantage to offset resource variability without noticeable impact on occupants.

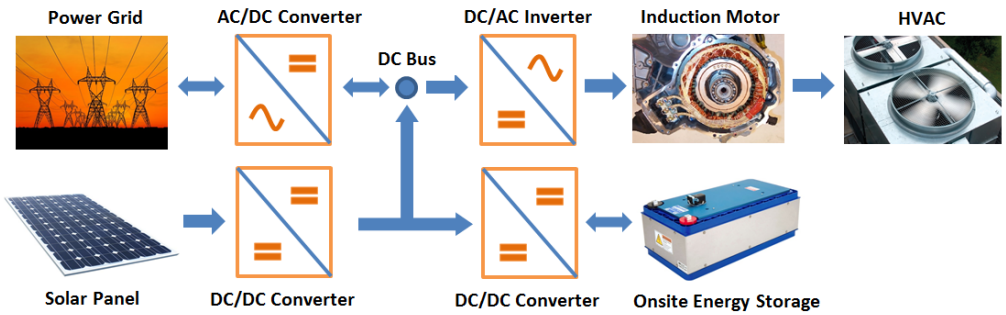

Figure 1.3. Energy flow inside a building with various types of converters that may be utilized to implement dynamic energy filtering.

A fundamental advantage of HVAC adjustment for effective dynamic thermal storage is that it is relatively easy to implement. Conventional building energy management systems and thermostats are designed to perform in slow control loops, on time scales of minutes. HVAC adjustment can use time-

scale separation and stay away from this "effective dc" loop action. In this sense, an ac feedforward signal is injected into a drive to adjust power flow on fast time scales, while avoiding interference on slow time scales. The average performance of the HVAC system remains intact, and the fast adjustment can be made transparent to users.

1.4.3. Curtailed PV power

Instead of using storage elements or creative alternatives such as dynamic load compensation with HVAC, PV variability can be partially reduced at the source, which in this analysis would mean at the photovoltaic module. This is the idea of PV curtailment based on operating reserve: sacrificing a bit of energy production for a reduction in uncertainty and variability. PV curtailment is not especially new, but it is typically used as a last resort when voltage rise on distribution lines becomes problematic [28]. Running with operating reserve is also not new and has been shown to be economical for wind energy [29], but poor implementation and worries about cost effectiveness may have previously limited its adoption for PV.

Cost in particular has typically been calculated with the mindset that PV is, and should be, treated as negative load. Therefore, curtailment has an opportunity cost equal to the cost of energy (below $0.05/kWh for systems with 25 year warranties) times the amount of energy sacrificed. This thesis will make the case in Chapter 4 that this is an incomplete picture since intermittency and inconsistent grid support capabilities mean that PV systems cannot be traded against most electricity generation resources. A comparable cost structure would include storage. Continuing cost reductions that take PV below cost parity introduce more direct opportunities for mitigating intermittency and providing active grid support. Chapter 4 will discuss how decreases in PV system costs can be leveraged against storage and grid support to provide "true" system-level cost parity comparable to large, cycling utility plants.

Curtailment has typically been treated as an ad-hoc solution to problems such as overvoltage [30]. It has been done out of necessity and therefore only affects periods of high or peak power output. It has also been unidirectional – able to back off of power production, but unable to provide additional power capability. The proposed method of operating reserve curtailment provides both positive and negative operating headroom, enables variability reduction throughout the full solar day, and does not restrict overvoltage protection algorithms. If implemented properly, PV curtailment with operating reserve could economically transform PV into a grid resource rather than a grid nuisance and enable deeper penetration of PV without destabilizing the grid. Chapter 5 details such a proposed operating reserve curtailment implementation.

2. High-speed Solar Data

A large portion of the results in this thesis are either derived from direct analysis of solar data or simulations that depend upon it. Therefore, it is imperative to discuss the origin of the high-speed solar data set used, the processing methods from which the useable metrics were derived, and the assumptions made in estimating high-speed changes in solar power. After all, photovoltaic arrays and panels are typically connected through maximum power point (MPP) controllers to the grid, and it is thus the variability of the MPP power that is truly seen by the grid or a net-zero building. In addition, the raw data contained numerous imperfections and inconsistencies that presented processing challenges, so the assumptions made as well as approaches used in creating a continuous, useable data set will be presented. Finally, the solar data represents a valuable resource, not only for this thesis work, but potentially for numerous others interested in the real-life, long-term, high-frequency solar data. For this reason, the essential content is slated for eventual publication, and the additional processing steps performed on the raw data are presented.

2.1. Data acquisition history

Professor Robert Pilawa of the University of Illinois Urbana-Champaign and his students designed and implemented a fast solar data acquisition setup in 2012 [31]. While [31] describes the experimental setup in more depth, here is a summary as it pertains to this work: During data collection, two, identical, rooftop-mounted, 20 W, PV panels, connected to two different meters, were placed side by side to eliminate spatial variation as much as possible. One meter was a Keithley 2420 that performed a sweep across the current-voltage (I-V) curve every 2.5-3.9 seconds, and the other was an Agilent 34410A that recorded short-circuit current at 5 kHz. The data acquisition mechanism is depicted in Figure 2.1. The sweeps from the Keithley ("slow") meter enable us to calculate open-circuit voltage (V_{OC}), short-circuit current, and MPP voltage, current, and power (V_{MPP}, I_{MPP}, P_{MPP}). The Agilent ("fast" or "high-speed") data provides high-frequency short-circuit current readings (I_{SC}) that, as will be shown, can be used to calculate high-frequency changes in the available power. To clarify, both meters measured short-circuit current, but in this thesis I_{SC} will almost always refer to the fast data. Slow short-circuit current data was used for verification of measurement accuracy against the fast meter and as a check of instrument synchronization.

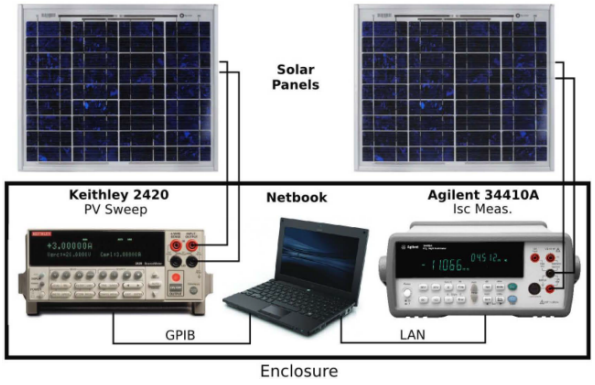

Figure 2.1. Solar data acquisition hardware setup [31].

2.2. Capturing all possible dynamics

Five kHz short-circuit data was recorded by the fast meter to ensure that all possible dynamics were captured. The explanation for why short-circuit current should capture (or at least indicate) the presence of fast, irradiance-based dynamics has been addressed [32]. When it comes to solar panels, the fastest dynamics are likely to be shadow-based, induced primarily by clouds and flying objects. Consider the fastest dynamic that could reasonably be expected: a shadow from a passing bird. A Canada Goose has a typical cruising speed of 40 mph (64 km/h) [33] and a minimum wing chord of about 0.4 m [34]. This means the shadow could pass on the order of $1/45^{th}$ of a second. By sampling at 5 kHz, even this hypothetical occurrence could be recreated with more than 110 data points. Atmospheric noise has the potential to induce still faster dynamics but given the broad area covered by solar arrays, the effects are assumed to average out by spatial variation and will not be specifically addressed in this thesis. Rigorously demonstrating that all of these dynamics were captured using numerical data is difficult. The following subsections will describe proposed solutions that rely upon knowledge of reasonably expected disturbances. They will show that even flickering shadows are fully captured at 100 Hz, and that faster dynamics are sufficiently insignificant as to not be considered.

2.2.1. Demonstrating smooth dynamics during characteristically noisy period

The dominant and most frequent dynamics in solar data, other than basic diurnal variation, are caused by passing clouds, so the first and simplest test is to visually ensure that even the most rapid transients are captured by the fast meter. That is to say that enough samples were taken such that the original signal could be accurately recreated, which would be evident if the data were “smooth” and did not contain visual jumps or discontinuities between samples. To demonstrate that indeed the sampling rate is sufficient, one of the dynamic days in the entire data set, namely March 31^{st}, 2013, is closely investigated in Figure 2.2. On this day, the solar panels experienced intermittent cloud cover and rapid

ramp rates as seen in the top image of Figure 2.2. The subsequent images depict some of the most dynamic subsets of data from that day to demonstrate that even during some of the most variable moments, all possible dynamics were captured in their entirety. In fact, the bottom sub-figure in this case still contains 100,000 data points, providing an exceptionally “smooth” recreation of the analog irradiance change.

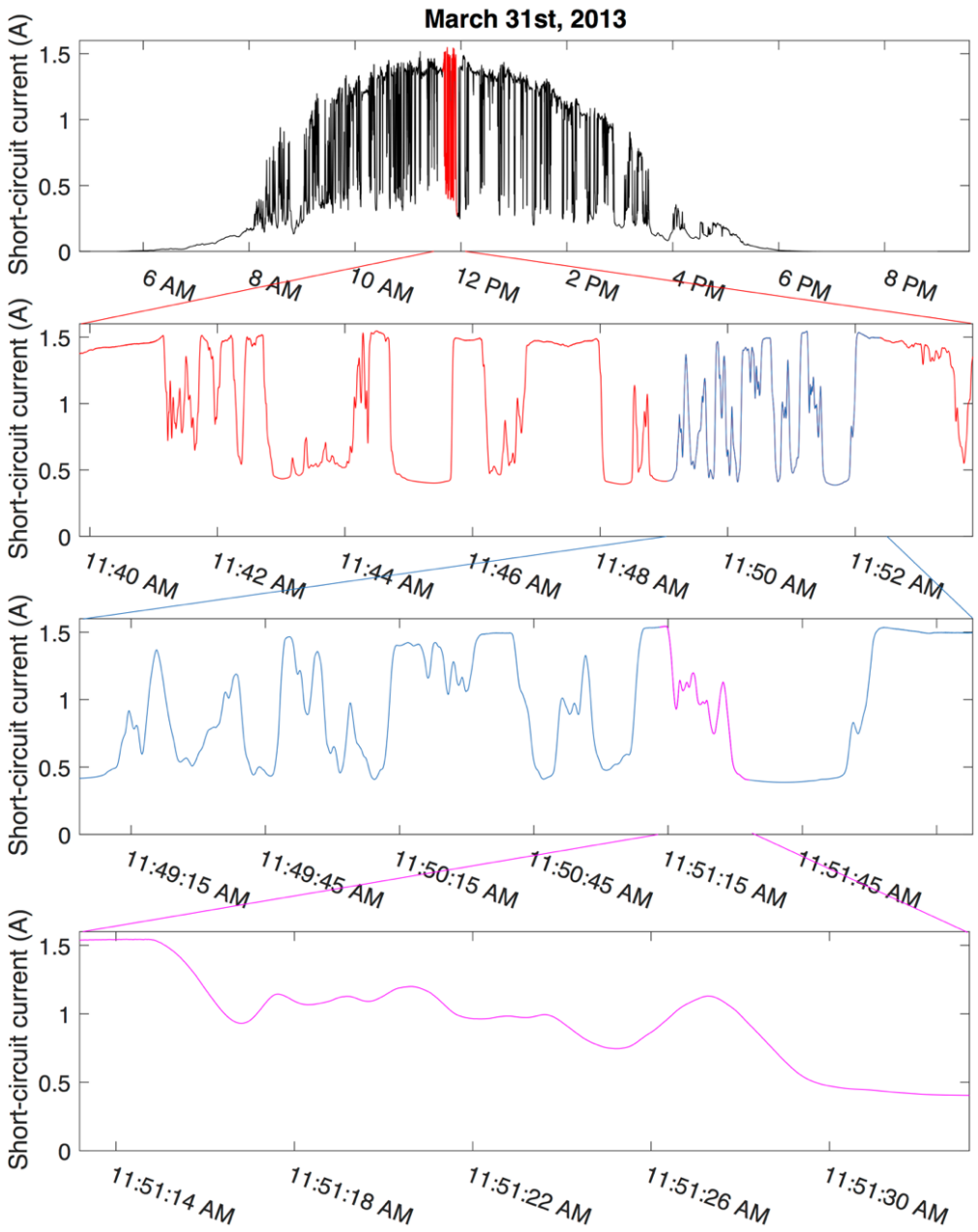

Figure 2.2. Sample day containing numerous rapid transients (top) and subsequent close-up views.

2.2.2. Verification during flickering shadows

Variability in solar irradiance can arise from sources other than clouds. While typically less frequent, the fastest dynamics are almost always caused by the flickering shadows of large bugs, birds, or airplanes passing between the panel and the sun. In order to more easily identify their occurrence, a high-pass Butterworth filter was applied to the raw, short-circuit current data (thick, blue line in Figure 2.3) and any ultra-narrow spikes were singled out. The spikes of interest do not have the characteristic curves on either side; such instances are a byproduct of a nonideal filter applied to rapid cloud transients. Example power dips of interest are circled in Figure 2.3 and appear as blips on moderate time scales (seconds to hours). Nevertheless, zooming in on these circled regions as in Figure 2.4 reveals that even the fine details of these transients are fully captured at 5 kHz. Instance #4 (Figure 2.4 on right) reveals four local minima that might be a result of a bird flying across the four columns of cells on the solar panel tested. While a 100 Hz subsampling does not capture these cell-level dynamics, it does capture the panel-level power dip with 3-4 points. From a panel energy production perspective, this is shown to be sufficient in Section 2.2.3.

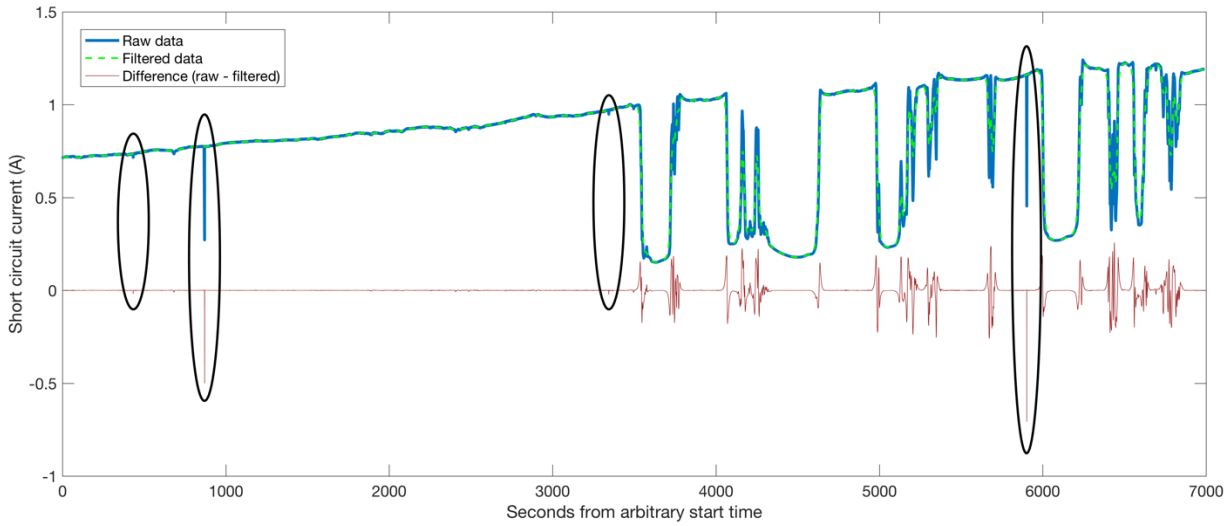

Figure 2.3. Sample solar data from July 16th, 2013 containing multiple, very rapid dips in power output (circled).

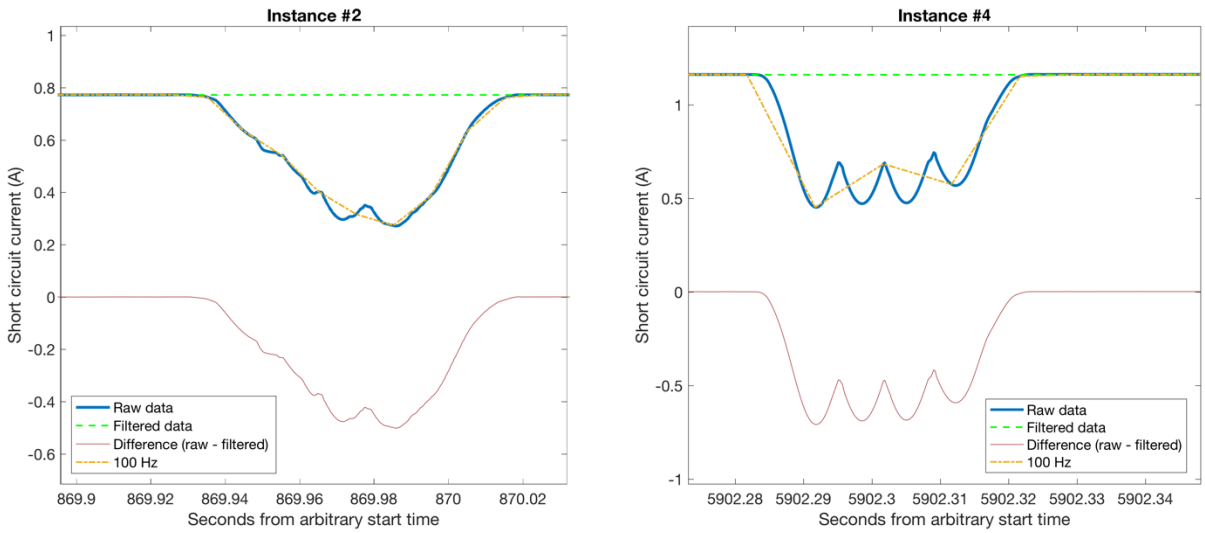

Figure 2.4. Highly zoomed-in views of the two most significant circled instances from Figure 2.3.

2.2.3. Investigation of dynamics in terms of potential energy loss

In section 2.2.2, the fastest expected class of shading dynamics were easily captured by a 5 kHz signal, and could largely be recreated with a sampling frequency of just 100 Hz. The question then becomes: Are there unknown sources of dynamics in solar power, and even if they exist, are they significant enough to be worth caring about? For example, atmospheric noise was mentioned in Section 2.2, but if its effect on solar power output does not meaningfully change the potential output power, then arguably, it is not worth tracking. Up to this point, high-speed variations were observed in the short-circuit current, but [32] argues that at least to first order, high-speed variations in power can be obtained from the high-frequency short-circuit data in conjunction with slower I-V sweep data. The full process will not be outlined here as this can be found in [32]; only the result is presented here. Assuming that a maximum power point tracker (MPPT) with constant update rate is used to maximize power output from a PV panel, then fast dynamics will result in decreased power output until the MPPT updates to the new MPP voltage. The cumulative energy missed during these periods is summed for a given 10 day sample as discussed in Section 2.3.1. Then, the energy sacrificed for a given MPPT update rate is divided by the total possible energy available (assumed to be the same as the MPP measured at 5 kHz). This ratio is plotted against the given update rates in Figure 2.5. Note that if any dynamics therefore exist above 100 Hz, for example, the energy sacrificed will only be about 1 part in 4000. At this point, the potential energy lost or gained by knowing the highest frequency variation is negligible. Perfect insight into the analog variations would only amount to about $0.35 of energy production value for a 250 W panel over its lifetime [32]. Therefore, what meaningful irradiance dynamics exist are

arguably captured completely with 100 Hz data, and any additional high-speed dynamics are not worth investigating for MPPT purposes.

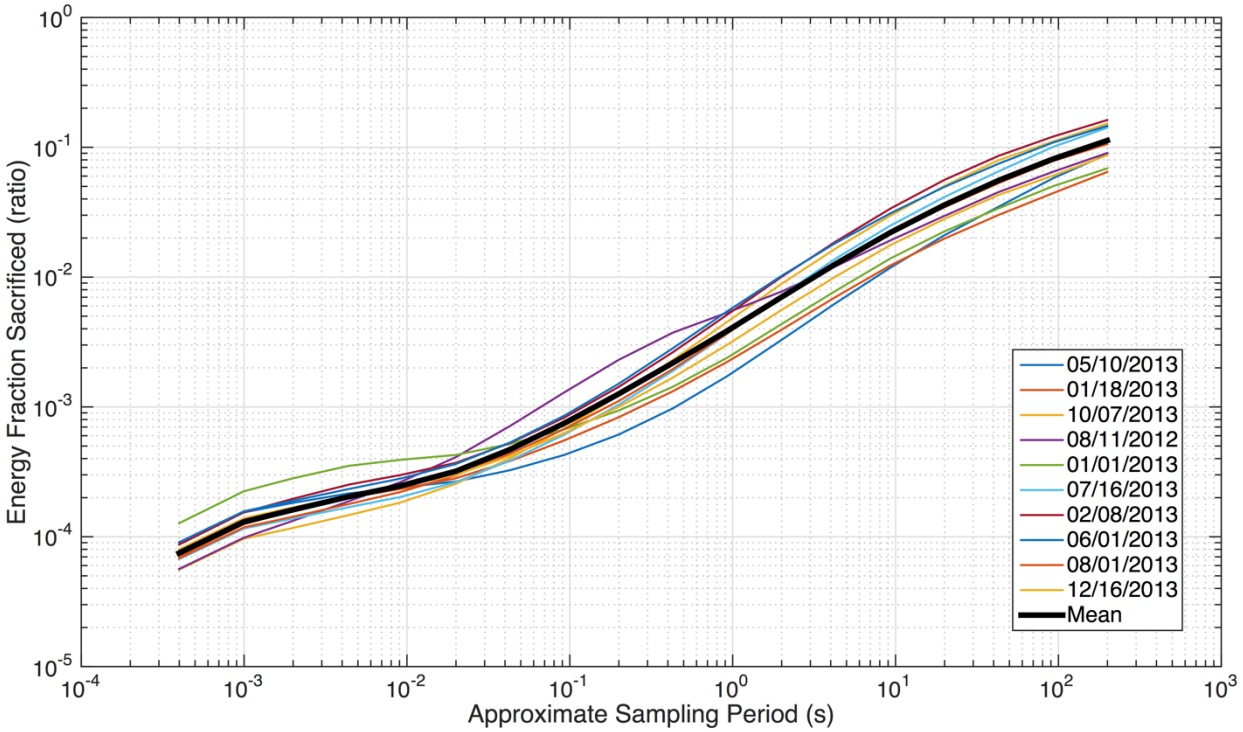

Figure 2.5. Modeled energy sacrifice of 10, 10-day samples with varying MPPT update rates and mean in bolded black. Entries in legend represent final day in 10-day series.

While perhaps less insightful to power engineers than sacrificed energy, fast Fourier transform (FFT) analysis of three very different days corroborated the 100 Hz conclusion. Figure 2.6 depicts the FFTs of a cloudless (smooth) day, a largely overcast (noisy) day, and a day with a cloudless morning and partly cloudy afternoon (partially noisy). Each has differing characteristics at lower frequencies, but above 100 Hz (or even 50 Hz) the frequency content is well below one part in one million with the exception of the 180 Hz coupled grid harmonic. At these scales, frequency content is effectively negligible and is on the order of fine measurement accuracy anyway.

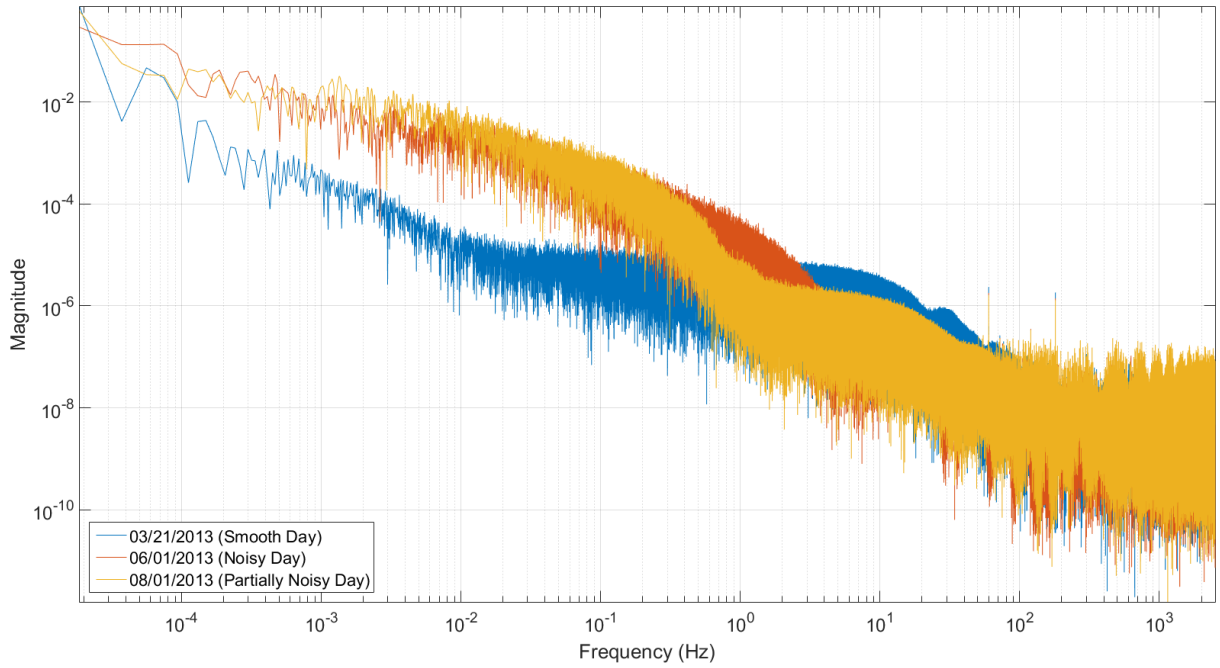

Figure 2.6. Full-day FFTs of 5 kHz short-circuit current for three different days.

2.3. Data processing challenges and approaches

The raw data set, as the name implies, was not immediately conducive to analysis. Missing data, formatting inconsistencies, and data rate variability were the primary obstacles. More specific details, along with the strategies used to correct or avoid these unexpected obstacles, are outlined in the following sections. Additionally, the raw data did not directly provide us with the desired parameters, namely high-frequency values for the maximum power point (MPP) power. As a first step toward this end, the final subsection will address the procedure used to calculate slow MPP values from current-voltage (I-V) sweeps.

2.3.1. Missing data

The first problem encountered was that of local missing data or non-sequitur time stamps. Such gaps are to be expected from real-life data sets due to equipment glitches or failures, instances where the code was updated, or other incidences. The first step to address this problem was to identify and flag missing or unexpected data. This was accomplished by computer code that recorded any instances where actual timestamps did not fall within windows of reasonably expected timestamps. A sample of the output data is shown in Figure 2.7 with red boxes indicating missing segments. A partial day is missing for the afternoon of March 28th, 2013, and a full day is missing on April 12th, 2013.

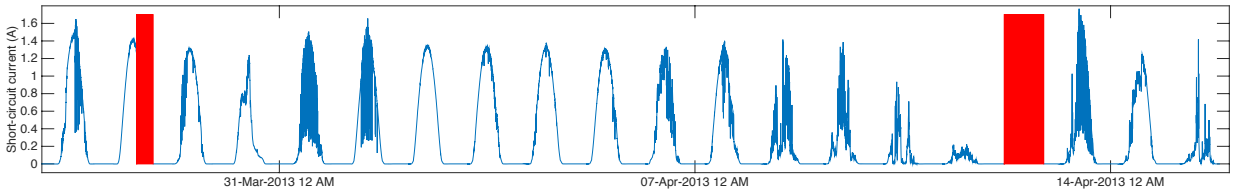

Figure 2.7. Solar panel short-circuit current vs. time with highlighted missing data segments.

Suitable data substitutions from other portions of the data set are discussed in Table 2.1, but for the energy sacrifice analysis of Section 2.2.3, a different approach was taken. Ten different, randomly selected, non-overlapping, 10-day samples (100 total days) were taken from the roughly 500 days of data to obtain a representative sample of long-term solar data. This was accomplished by randomly selecting a starting day, and then proceeding to use that day and the nine subsequent days, provided that none of them overlapped with other samples or contained a segment of missing data. For example, if the first random number generated corresponded to March 31st, 2013, then the segment of data spanning March 31st, 2013 to April 9th, 2013 would be used since Figure 2.7 indicates that it does not contain a segment of missing data. As a counter example, if the next random number happened to correspond to April 7th, 2013, then the selection would be invalidated and a new random starting date selected since the segment beginning with April 7th overlaps with the first sample (and contains missing data for April 12th, 2013). This process was selected because it contained representative segments from all times of year, incorporated long-term effects that might appear in multi-day weather patterns, and enabled direct use of the solar data without additional complications or uncertainty.

2.3.2. Substituted data for public use

The long-term, high-speed PV data set is useful for analysis in this thesis, but it has long been a goal to prepare a version for public use. The finalized data set provides one continuous year of data that can be used in simulations to accurately represent real-life power outputs from a panel. No matter the start date chosen, though, no 365 consecutive days were without some missing data segments. Dismissing the work-around mentioned in Section 2.3.1, missing or incomplete days thus had to be substituted. To avoid introducing sudden changes or stark weather pattern contrasts, whole days were substituted even when partial data was available. Table 2.1 summarizes all incomplete days between November 1st, 2012 and November 1st, 2013, the portion and type of data missing, and the respective daily substitutes.

Table 2.1. Summary of Days with Missing Data and Substitutions Used

Missing Day	Part Missing	Missing Slow and/or Fast Meter Data	Replacement Day	Scaling Factor
11/23/2012	1 min section	Fast	11/23/2013	1.0000000
12/02/2012	All day	Slow	12/02/2013	1.0000000
02/26/2013	Partial day	Slow	10/05/2012	1.0000000
02/27/2013	Morning	Both	10/02/2012	0.9163347
03/28/2013	Afternoon	Both	03/21/2013	1.0405904
04/12/2013	All day	Both	08/13/2013	1.0000000
07/27/2013	Partial day	Slow	07/27/2012	1.0000000
08/05/2013	Partial day	Slow	08/05/2012	1.0000000
08/29/2013	Partial day	Slow	08/12/2012	1.0000000
08/31/2013	Partial day	Slow	08/20/2012	1.0000000
09/02/2013	Partial day	Slow	08/10/2012	1.0000000
10/14/2013	Partial day	Both	10/25/2012	1.0000000

Substitute days were chosen with the following preference:

1. If a non-repeated, complete day (containing all data) was available from one year either prior or subsequent, this day was selected as a replacement.
2. Else, if a non-repeated, complete day was available from an equidistant time away from the Winter or Summer solstice, this day was selected as a replacement. In other words, the replacement day would be as many days after the solstice as the original was before it, or vice versa.
3. Else, days with similar historic weather patterns and temperatures were selected with a preference for days close to the original date (in a prior or subsequent year) and secondary preference for days close to an equidistant Winter or Summer solstice counterpart (as in 2).

Typically, unity scaling factors were chosen, but in cases where partial data existed, substitute data could be scaled slightly to better match the original data.

2.3.3. Data synchronization

In short, data synchronization was accomplished by aligning data with matching, corresponding time stamps. In reality, however, the process was a bit more involved. First of all, there was no consistent file length, duration, or number of data points per file. For example, the fast short-circuit current data varied in rate between about 5010 Hz to 5014 Hz with the first file recording at about 5250 Hz and time stamps spanning between 57 and 59 seconds. Setting a nominal increment of 200 μs (inverse of 5 kHz) therefore caused significant offsets over the tens of thousands of seconds recorded each day. To resolve this offset and enable synchronization with the slow sweep data, the computer program had its own master clock which it would increment with the mean period T_{mean} between data samples as determined by the following simple equation:

$$\boldsymbol{T_{mean}} = \frac{\boldsymbol{t_{end} - t_{start}}}{\boldsymbol{\#\ samples\ in\ file}} \tag{2.1}$$

While time stamps only had precision down to 0.01 s, this was overshadowed by the fact that the slow I-V sweeps did not identify time stamps between regions of the sweep. That is to say that the open-circuit voltage, MPP values, and short-circuit current measurements took place ambiguously within the 2.5-3.9 second duration of each sweep.

To improve synchronization of data, raw short-circuit data from both fast and slow sets were compared over a ± 1 s window. Since we would expect the short-circuit current to be the same on both panels (the one measured by the fast meter and the one measured by the slow meter), it was reasonable to assume that similar values should be recorded at the same instant in time, and thus we could adjust the slow meter time stamp to better match the interpolated time stamp of the fast meter. This was accomplished by maximizing the correlation of the two current measurements over the course of each day. If n is the total number of points in a day and m is the maximum sample offset to be considered, then the most likely timestamp offset for the slow meter will be the value of t_{offset} that maximizes

$$\boldsymbol{T_{offset}} = \mathbf{max}\left[\sum_{\boldsymbol{t=m}}^{\boldsymbol{t=n-m}} \boldsymbol{I_{SCslow}(t)} \times \boldsymbol{I_{SCfast}(t - t_{offset})}\right], \qquad \boldsymbol{-m < t_{offset} < m} \tag{2.2}$$

The effectiveness of this calculation is presented at seven equally spaced points throughout each day to visually verify that the calculated offset improved overall alignment of short-circuit data in time. A sample of two of the seven windows from 3/31/2013 is shown in Figure 2.8. These samples visually depict better alignment of data from the two separate meters during periods of rapid irradiance changes. The solid blue curve represents the high-speed short-circuit data, the red dashed line represents the slow meter short-circuit current with original timestamps and the green dotted line

represents measurements from the slow meter with optimal offset. In an ideal case, the apparent vertices of the slow meter would lie precisely on top of the smooth, high-speed data as if being sampled from the same data set. Note that this analysis was only performed for the two short-circuit measurements. I-V sweep data and open-circuit voltage would have additional offsets as they were recorded subsequent to the short-circuit current on the slow meter. However, aligning these parameters using the same method would assume that increases and decreases correlate to increases and decreases in short-circuit current, which may not always be true, especially given the variability of where within the I-V sweep MPP values occurred.

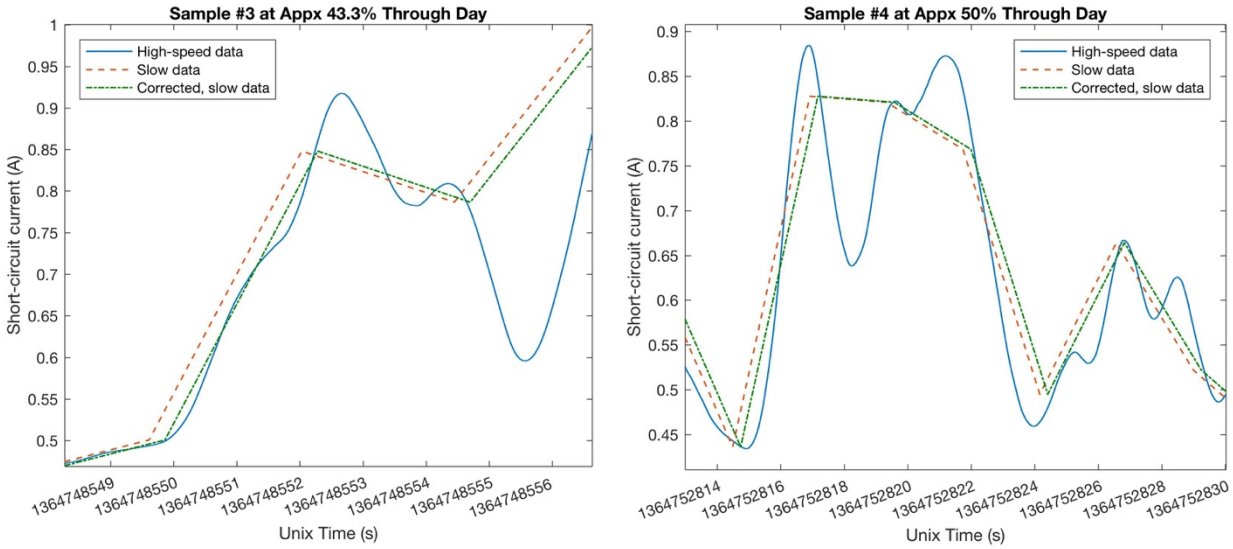

Figure 2.8. Two sample windows of data alignment from March 31st, 2013 showing better data alignment with time offset.

2.3.4. Parameter calculation

Even after all of the data was synchronized and missing data segments filled, some of the desired parameters had to be calculated before they were used. The 5 kHz data came in an immediately usable form, but the slow I-V curve data required specific processing techniques in order to obtain short-circuit current, open-circuit voltage, MPP current, MPP voltage, and MPP power values. Slow short-circuit current data consists of three data points near 0 V, the square symbols in Figure 2.9. Open-circuit voltages (V_{OC}) were obtained from the sweeps that crossed the voltage axis, the triangle symbols in Figure 2.9. MPP voltage, current, and power took the most processing. In Figure 2.9, the MPP region contains 100 points on the "knee" of the I-V curve. As can be seen in Figure 2.10, the measurements contain a combination of high-frequency fluctuations and measurement noise. Simply picking the point with the peak value can lead to misleading and inaccurate MPP values. To alleviate this, a 4th-order polynomial least-squares fit was applied to the data to capture the overall nature of the sweep.

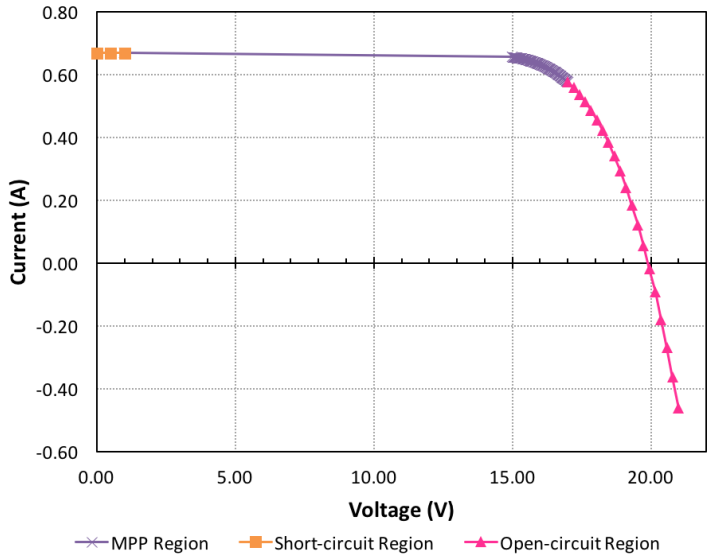

Figure 2.9. Slow, current-voltage (I-V), full-range sweep containing data points near the short-circuit, open-circuit, and maximum power point region.

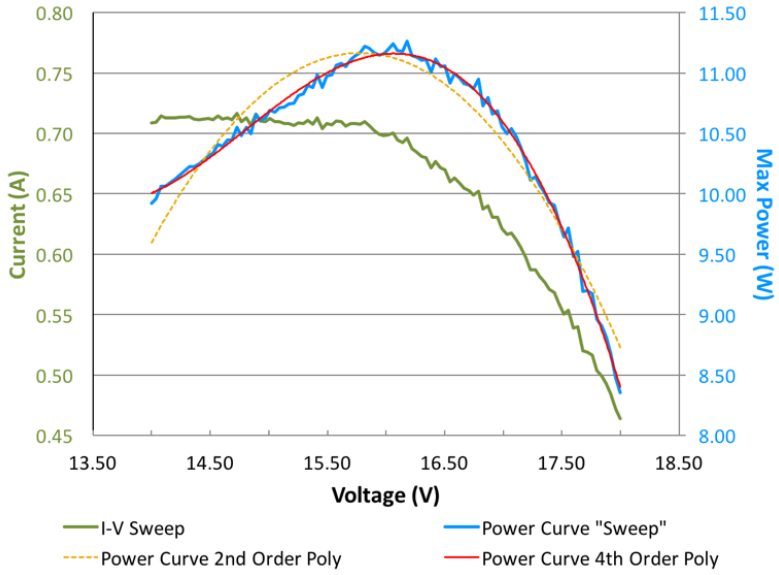

Figure 2.10. Slow I-V sweep in MPP region and max power curve with polynomial least squares fits.

Implementing a 4th-order fit instead of the 2nd-order polynomial used in [31] increased the regression coefficient from R^2 = 0.95 to R^2 = 0.995 for a typical MPP sweep. Higher-order polynomials or other functions may be used instead, but the 4th-order polynomial captures the expected shape of the power curve well. Rather than solving for the peak algebraically, it was computationally more efficient to evaluate the polynomial function at 500 equally spaced points over the same range of voltages as the original MPP region and then select the maximum value from this finely discretized set.

For instances where a peak value was not found, the polynomial kept increasing or decreasing monotonically because the slow meter missed the MPP. In this case, the maximum interpolated value (an endpoint) was chosen as the MPP. An example is provided in Figure 2.11 in which three consecutive MPP sweeps are shown with the middle (orange) sweep failing to span the peak power value. This failure is likely due to a sudden drop in irradiance following a previously increasing trend. According to the procedure mentioned above, the MPP power would be that associated with the power at the left end of the middle curve, or 16.00 V in this specific instance. Sometimes the fluctuations were so fast that within a single sweep, the polynomial approximation generated two peaks (or potentially more if a higher-order polynomial were to be used). Figure 2.12 exemplifies such a scenario, where the polynomial was a poor approximation of the raw data. In cases like this, the maximum value of the raw sweep data (marked) was chosen instead of the polynomial peak. More generally, polynomial approximations with $R^2 < 0.99$ were deemed invalid and the raw data peak used instead. The polynomial fit is only beneficial if it closely represents the original data. Thus, the instance of two peaks in Figure 2.12 would be ruled out due to a poor polynomial fit. After computing values from the slow meter data, the results were synchronized with the fast meter measurements using time stamps recorded in both data sets.

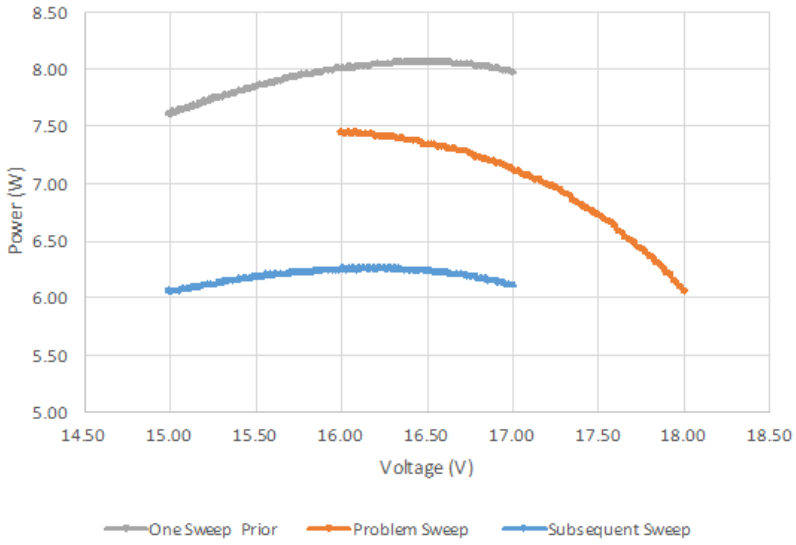

Figure 2.11. Three consecutive MPP power curve sweeps with the middle sweep missing the MPP.

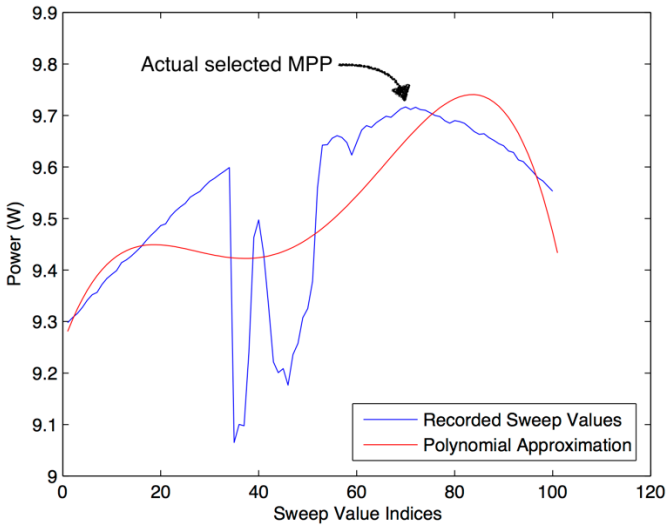

Figure 2.12. Rapid transient during MPP sweep and associated poor fit polynomial approximation.

2.4. Slow meter current saturation and action taken

When verifying the data synchronization in Section 2.3.3, it was observed that slow meter I-V sweep currents saturated at approximately 1.35-1.375 A despite simultaneous fast meter short-circuit measurements recording higher currents, up to almost 1.8 A at times. Saturation affects about half of the recorded days after April 2nd, 2013, and was likely a result of an improper range setting. This deduction is backed by two pieces of evidence. First, the beginning of the inaccurate data coincides with a break in the data during which data recording formats were changed. Secondly, the saturation point is just slightly greater than the rated peak current of 1.29 A. This means the 1.35 A set-point would be suitable for most instances except for when the sun appeared between clouds on bright, partly cloudy days. In the short term, nothing much can be done about the inaccurate data. Results of Section 2.2.3 might be slightly skewed and could be recalculated with only days unaffected by the saturation. Longer term, the proposed published data set already excludes any potentially inaccurate sweep data and a repeat experiment for data acquisition is encouraged.

2.5. Public and auxiliary uses for PV data set

The primary purpose of the high-speed solar data, as it pertains to this thesis, is to obtain a realistic data set to better model effects of solar power variability. As mentioned, though, a cleaned-up version of the long-term PV data set is intended for public use. Thanks to lessons learned through utilization of the high-speed data, a few changes were made. Time stamps and file length were made more consistent across the slow and fast meter data; sweep data was simplified down to the key points of interest such as MPP current and open-circuit voltage; and thanks to the analysis performed on the dynamic content,

high-speed data could be down-sampled (after passing a median filter to eliminate measurement noise) to just 100 Hz to reduce file sizes without losing substantive information.

As in Section 2.2.2, finding the fastest dynamics took considerable effort. The Butterworth filter used to isolate rapid changes had to be applied to billions of points per day and anomalies had to be identified manually. With the down-sampled data set, this search becomes much easier. The median filter applied before down-sampling eliminates presumed measurement and atmospheric noise enabling a computationally simple derivative to be taken. Strings of data with large derivatives should indicate a rapid dynamic and can be further investigated.

3. Dynamic HVAC Load Compensation

Dynamic load compensation is a variability-reducing alternative to chemical storage. It can be relatively cheap and easy to implement, provide effective grid inertia, and reduce variability of onsite PV power variations [35], [36]. When heating, ventilation, and air conditioning (HVAC) systems are to be used as the load medium, though, dynamic load compensation also has its limits. This chapter focuses on variable speed drives involved in dynamic HVAC compensation with multiple portions having been previously published in [35], [36].

HVAC-implemented energy resource filtering has both upper and lower frequency band bounds beyond which it should not operate. The lower frequency limit, meaning the lowest update rate for HVAC speed and power commands, is established to shield building users from substantial temperature swings, ideally keeping variations imperceptible. An upper frequency limit, meaning the highest update rate for HVAC speed and power commands, is needed such that the following conditions are met: (1) HVAC drives are capable of responding, (2) undue wear and tear is not induced on drives or mechanical parts, and (3) update rates do not create discomforting audible pitch or amplitude changes.

Frequency domain analysis is performed to illustrate available filtering potential, and approximate upper and lower frequency bounds are discussed. This analysis utilizes PV data from the high-frequency data set presented in Chapter 2. If the HVAC system can effectively filter power usage over a useful frequency band, the power grid will then be better able to provide and absorb slower changes in demand to balance the longer-term building energy flow. Conventional onsite energy storage could absorb additional power shortages and surpluses where HVAC falls short, such as changes extending outside of frequency band boundaries. As a result, the electric grid benefits from a much slower varied energy demand, and conventional energy storage size is substantially reduced. This chapter will investigate what high-frequency variations there are to remove and how they were determined. It will also present the fan drive experiment performed and the bandwidth permissible for filtering capabilities. Finally, simulated filtering capability of dynamically controlled HVAC systems is presented for various cases with differing sizes of PV installations and HVAC limitations.

3.1. Desired solar power variation absorption

In an ideal scenario where dynamic HVAC load compensation has infinite storage capacity and instantaneous response times, fixed power targets can be set, and solar energy variation can be filtered completely by the HVAC system (without being imposed on the power grid). In other words, the ideal

system would store or release building thermal energy via the HVAC system so that the combined power of the PV system and HVAC perturbation would exactly match the desired power target at each moment. With the frequency domain analysis, we model the effects of an idealized HVAC system that offsets variations by passing the solar data through various low-pass filters, each with a different cut-off frequency, to obtain the desired power targets. For most of the analysis in this section, raw data came from June 15th, 2013, shown as day 1 (hours 0-16) in Figure 3.1.

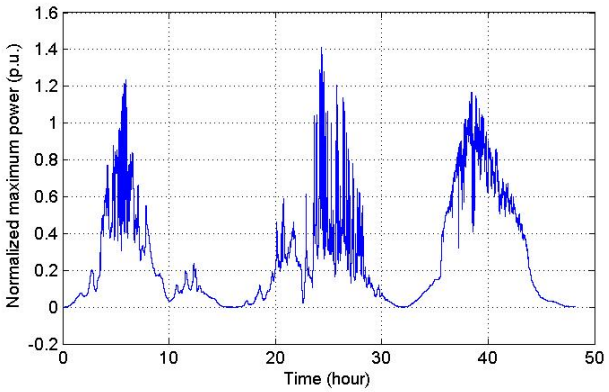

Figure 3.1. Solar power profile from June 15th-18th, 2013 (only 4 a.m. to 8 p.m. shown per day).

Figure **3.2** shows low-pass filtered solar panel power targets from June 15th, 2013 under filters with 1, 5, 15, and 30 min cut-off time constants. Power values are normalized to a cloud-free daily maximum.

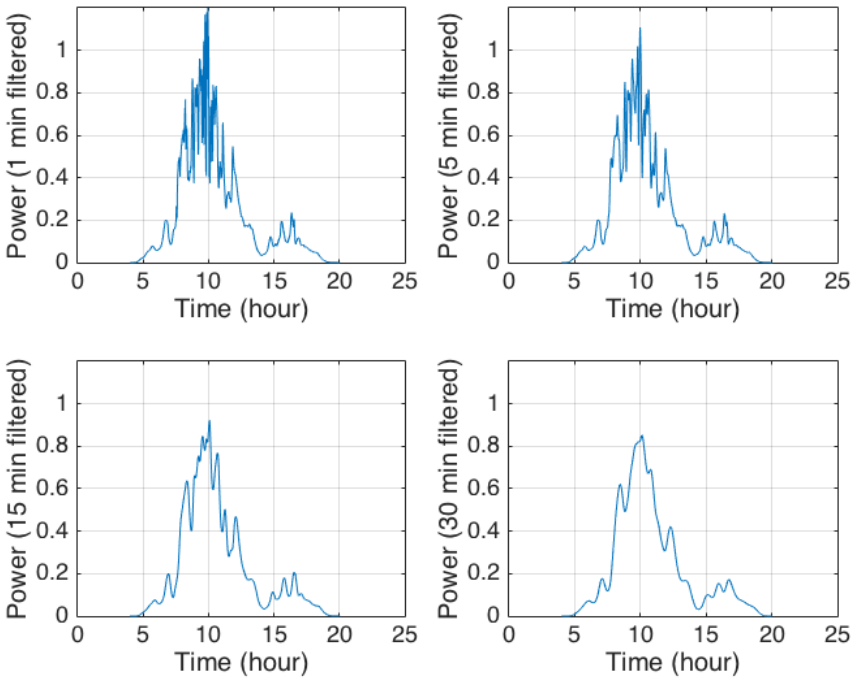

Figure 3.2. Ideal solar power profile seen from the grid after HVAC filtering effect.

Figure 3.3 shows the power that the ideal HVAC system would need to absorb or supply in order to realize the filtered outputs of Figure **3.2**. This power would be imposed on top of a baseline power consumption dictated by conventional thermostatic controls. A sample baseline profile and profile with dynamic filtering imposed on it are shown in Figure 3.4. In the figure, the profile is given in terms of commanded HVAC fan speeds, but the general idea is the same; increased speeds above the baseline correspond to positive power demand or power needing to be absorbed, while decreased speeds below the baseline profile correspond to negative power demand.

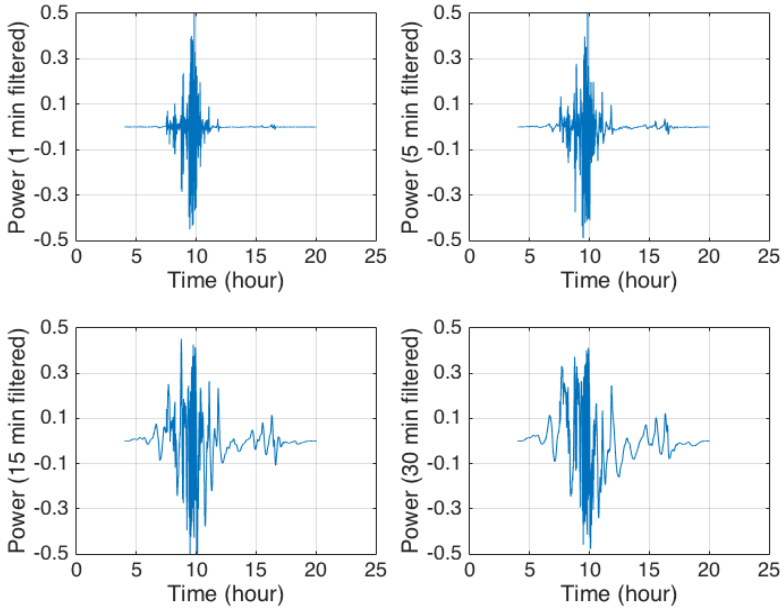

Figure 3.3. Solar power to be filtered by the HVAC systems.

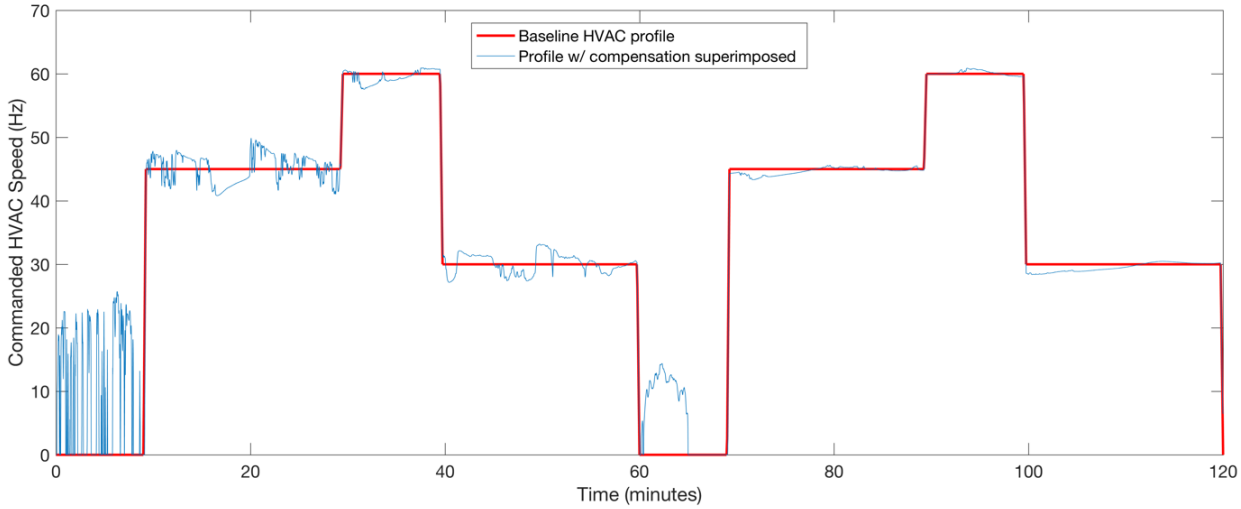

Figure 3.4. Fan drive speed profile without and with dynamic HVAC filtering superimposed.

In reality, HVAC systems have limited filtering capability, so a compromise between power demand and certainty of net power output is needed. By following the general or large-feature trends in the solar data, load compensation power demands are decreased, while still providing increased confidence that net power in the next moment will not vary drastically from its current level. Figure 3.5 illustrates the difference in filtering power required between two different set-point algorithms. In one, set points consist of Butterworth filter output with an upper cut-off point of 15 min, while in the other, 15 min sample-and-hold values (taken from the filtered data) constitute constant obligation set points. As would be expected, the constant obligation requires longer periods of increased power compensation when compared to the filtered power set point, especially in times of slower dynamics.

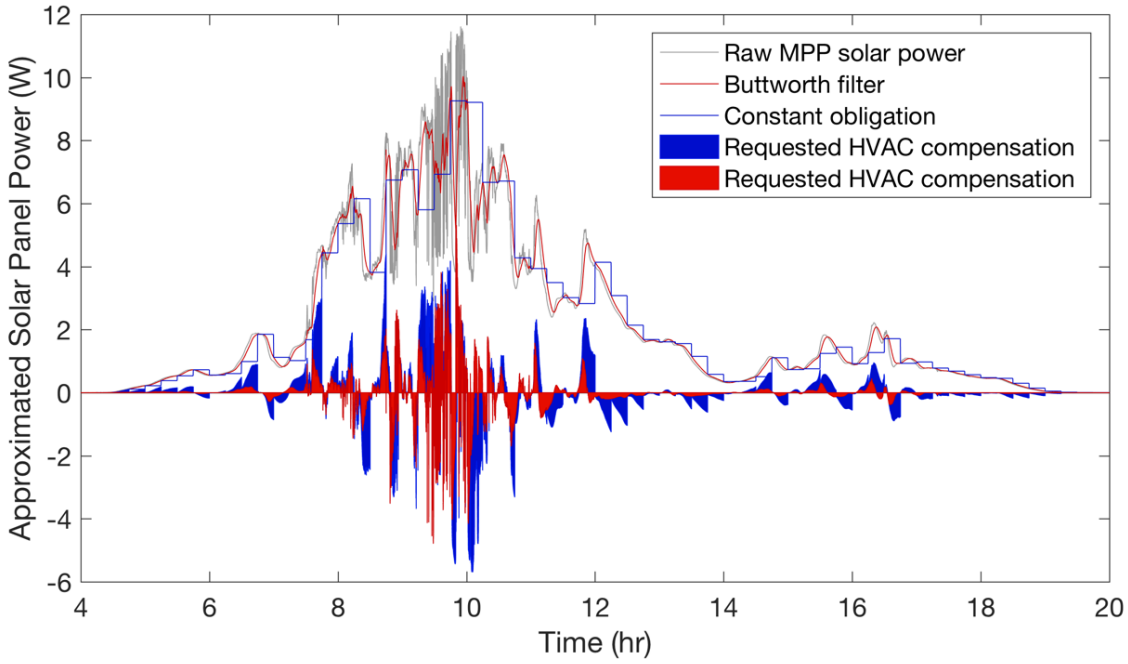

Figure 3.5. Filter power requested of HVAC compensation for June 15th, 2013.

Compensation in Figure 3.5 still neglects ramp rate, thermal, and acoustic limitations of the HVAC system. Such limitations and their effect are discussed in subsequent sections.

3.2. Scale model setup and fan-power/-speed profiling

A scale model HVAC test bed was implemented to demonstrate and validate the potential of an HVAC system to filter energy content. This proof of concept blower setup needed to be characterized to understand the relation between rotational speed and power consumed. During the experiment, acoustic variations were recorded and analyzed for later use. Once validated, scaled up filtering capabilities could be calculated given proper assumptions.

3.2.1. Small blower characterization

A small fan drive was used to follow scaled responses to various band-limited solar power profiles. Since the controller accepts fan-speeds as input and not power, a conversion was necessary. For our experiment, the electrical synchronous fan drive speed ν in Hz and its power P in watts are related by

$$P(\nu) = 1.6266\times10^{-4}\nu^3 + 2.9997\times10^{-3}\nu^2 + 7.7925\times10^{-3}\nu + 7.8064 \quad (3.1)$$

where the coefficients were identified by a least squares fit as in Figure 3.6.

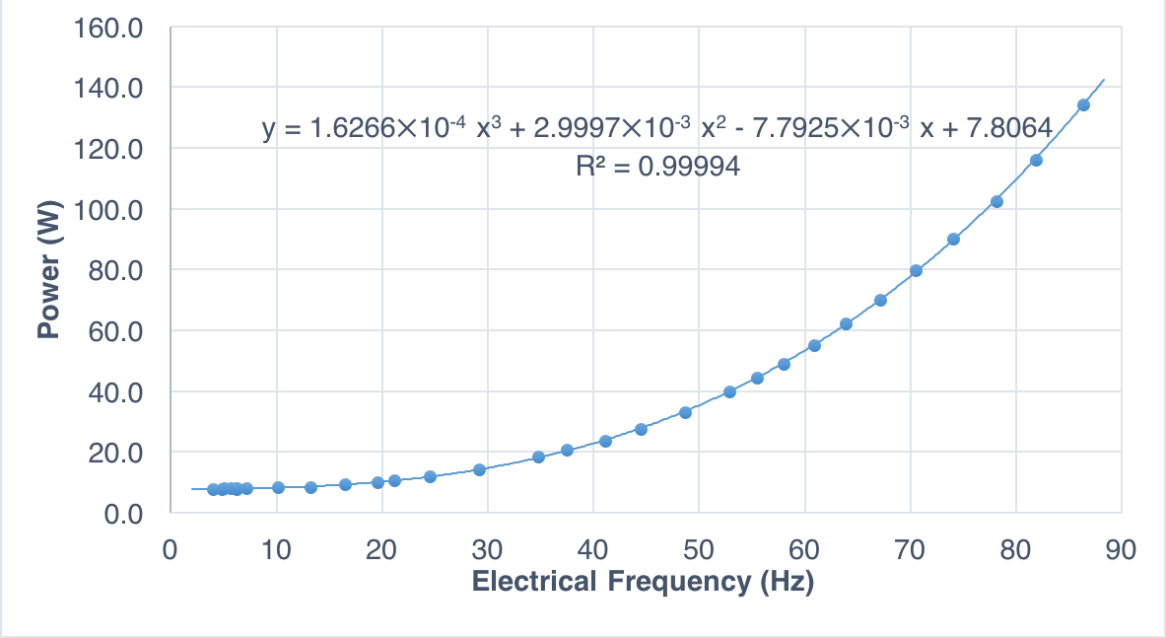

Figure 3.6. Small-scale motor blower power vs. electrical speed.

Acoustic effects of the fan drive were recorded with a high fidelity microphone to test whether machine speed update rates cause distracting sounds. Figure 3.7 shows the experimental setup. A 1/3 HP, three-phase, four-pole, induction machine was coupled with a fan blower. A Yaskawa CIMR-F7U23P7 drive was used to control the fan speed through frequency and voltage. The drive was externally programmed by a TI MSP430 microcontroller to adjust fan speed with a 0.02 s update rate to follow the solar power profiles with high fidelity.

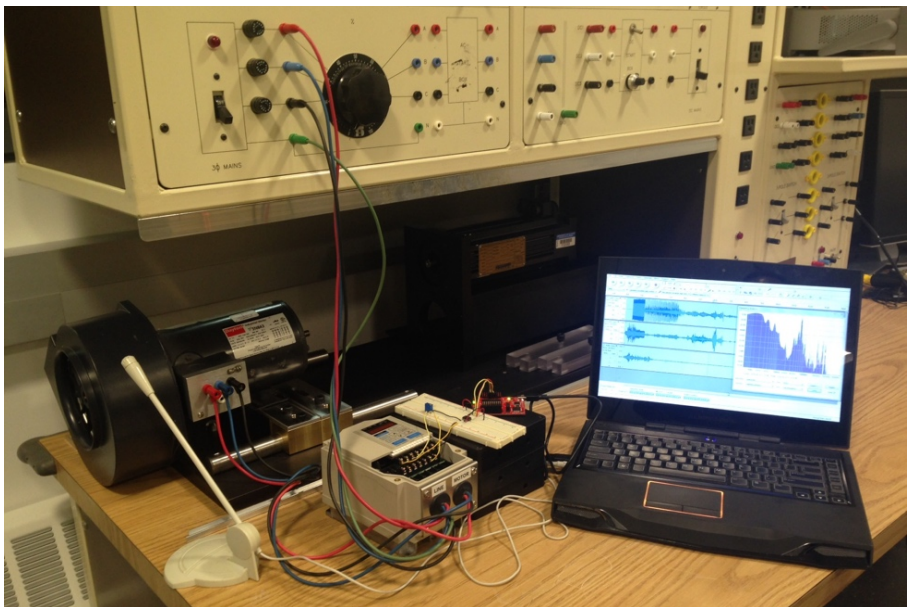

Figure 3.7. Experimental setup for recording acoustic effects of various fan speed profiles.

3.2.2. Scaling assumptions

Acoustic effects of the small-scale blower were recorded at unity scale to emulate the airflow through an individual vent in a room. The merits of this choice are discussed in Section 3.3.2. Electrically, blower power results were scaled up to building level before being fed into a full-scale, filtering-potential simulation. Scaling was assumed linear as a fraction of peak power both for the PV data and HVAC variable speed drives. It was assumed that both systems are fairly modular with increased capacity typically resulting from an increased number of units. This is a better approximation for PV systems than HVAC as centralized blowers are often much larger than the fan used in this experiment and may not scale exactly linearly. Peak building-level power values were based on projected power consumption of the Electrical and Computer Engineering Building (ECEB) with 1.5 MWp designed solar capacity [37] and about 18.6% of this peak power anticipated for average load conditions. Since ECEB is expected to be nearly net-zero, its average load should approximately equal the capacity factor of the installed PV generation for Illinois, and hence the estimate of 18.6% peak capacity [38].

3.3. Variation absorption capability

The limitation of any dynamic load compensation technique is that it requires full cooperation on the part of the load, which may or may not interfere with its effectiveness at performing the originally intended task. The absolute power capability is also a factor. If performance of the native task is prioritized over dynamic load compensation, then the capacity to absorb variability will be reduced. This will also be true if the load power is insufficient to meet the demanded compensation. Variable speed

drives in HVAC systems experience a number of such limitations. There are, of course, peak power limitations associated with the fastest possible fan drive speed available and minimum power limitations associated with variable speed drives operating at 0 Hz (off or standby mode). In our experiment, these limits were overshadowed by an allowable range of speeds associated with amplitude variation that is discussed in Section 3.3.1. Then there are ramp limits. Fans cannot accelerate or decelerate faster than a given rate for reasons discussed in Section 3.3.2. While ramp rates limit load compensation's upper frequency bound, thermal variation typically limits the lower frequency bound. Absorbing or "releasing" electrical energy into thermal energy alters the temperature of a building. Work by Cao [35] estimates that filtering capability associated with a 15 min cutoff filter or faster could be implemented in large structures without altering the temperature too greatly as to be noticeable by occupants.

3.3.1. Amplitude variance bounds

When more or less energy is dissipated into variable speed drives, airflows either increase or decrease relative to their baseline speed. These changes in airflow have differing acoustic amplitudes. Therefore, absolute minimum and maximum fan speeds were defined based on an objective of imperceptible acoustics. A series of acoustics tests, injecting 1 min sinusoidal speed commands with various amplitudes into the motor drive controller, were conducted. Taking 60 Hz as a baseline, the sinusoidal amplitudes vary ±5%, ±10%, …, ±45%. The respective recorded noise envelopes in dB are shown in Figure 3.8. Also shown is the peak-to-peak amplitude of each curve compared to the baseline magnitude to generate a normalized expectation about amplitude variations. As verified by subjective human hearing tests, the speed variation corresponding to 0 dB in Figure 3.8, or equivalently a peak-to-peak change equal to the baseline magnitude (±16%), seems to be imperceptible. This means that about 50 Hz and 70 Hz are appropriate minimum and maximum fan speed limits for a 60 Hz base. Note that this introduces a more stringent constraint on the overall HVAC filtering capability than the maximum and minimum power limits. Filtering capability with this narrower constraint is considered in the far right column in Table 3.1 in Section 3.4.

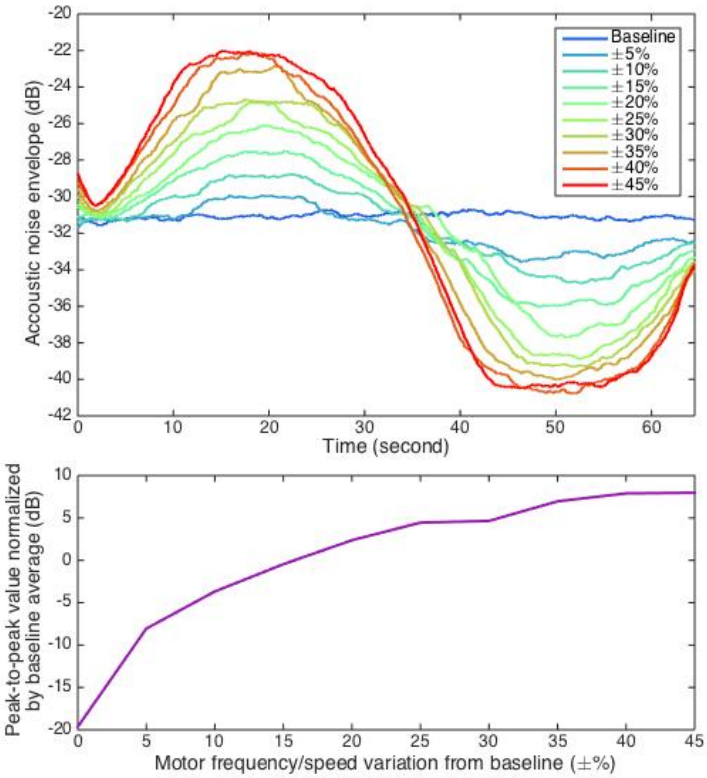

Figure 3.8. Acoustic noise amplitude (top) and relative amplitude change compared to baseline (bottom) for various sinusoidal fan speed profiles.

3.3.2. Ramp rate limit

In conventional, thermostatically controlled environments, HVAC blower motor drives normally operate at fixed frequencies as might be observed in red in Figure 3.4. Impose additional filtering dynamics, however, and the fan speed will likely vary constantly, much like the blue curve in Figure 3.4. If this variation is rapid enough it will attract unwanted attention from building occupants, so a ramp limit should be imposed to never allow commanded dynamics to exceed a certain rate. To determine this allowable limit, approximately 1 min of solar power data from June 15th, 2013 at 10:00 AM was used for audio analysis. This sample was chosen because it included a mix of relatively constant (±3%) and rapidly varying (±20%) power. The scenario tested was for a building in which 50% of the average power would come from solar and about 45% of this average load would be attributable to the HVAC system [26]. Various ramp rate limits were applied and the research team commented on which they found to be highly noticeable. In the end, the team agreed that a 9 Hz/s ramp-limited profile significantly reduced the attention drawn to the blower's operation, though they admitted that the changes would still probably be distracting if occupants were to focus on them. In this experiment, 9 Hz/s means that the motor drive would ramp from a standstill to peak speed (capped at about 90 Hz) in 10 s.

As previously mentioned in Section 3.2.2, unscaled acoustic measurements in this experiment were taken from a 0.5 m away. The idea was to emulate airflow out of a single vent, but in such a setup motor sounds dominate noise production. In contrast, motors and blowers in more realistic HVAC systems are distant from the occupants, hence dampening the sound of all but the changing air flow. Therefore, real ramp rate limits and amplitude limits could likely be relaxed, and a repeat experiment with a typical air vents and ducts is recommended. Still, initial results and subjective perspectives indicate that a 9 Hz/s frequency ramp appears to be a plausible upper limit. A commanded speed profile abiding by this limitation (in addition to the hard-set max/min limit) is shown as a dashed line in Figure 3.9 along with the purely capacity-limited speed profile. Note that the minimum and maximum values in effect in Figure 3.9 are 0% and ~120% of baseline speed (60 Hz), even over the course of just 1 min. Therefore, the linear frequency change limits are enforced any time the desired frequency change exceeds 9 Hz/sec.

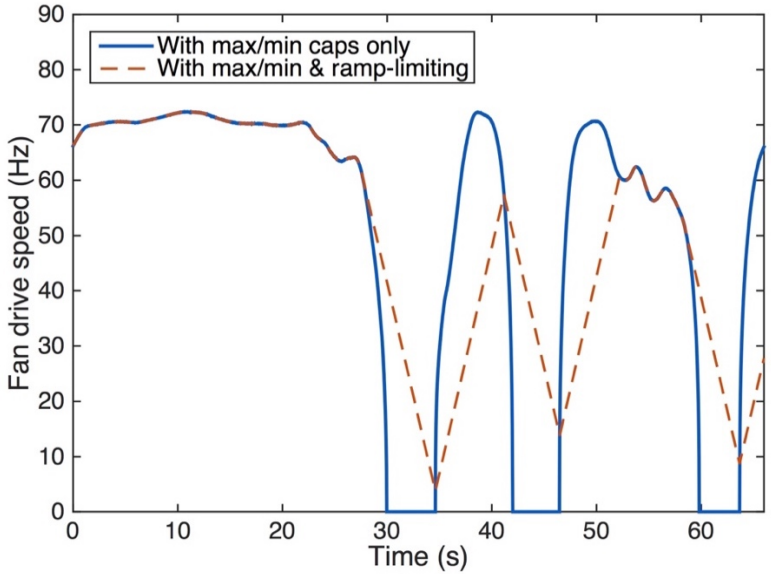

Figure 3.9. Commanded speed profile with speed caps and ramp-limiting.

An unfortunate side effect of ramp limiting is that during periods of rapid power fluctuation there are times during which the HVAC filter is slow enough to be counterproductive. This is easier to see in Figure 3.10 when the ramp limited power compensation (dotted orange line) is compared to the ideal power compensation (solid light gray curve). In such cases, a proportional-derivative (PD) control might produce better performance.

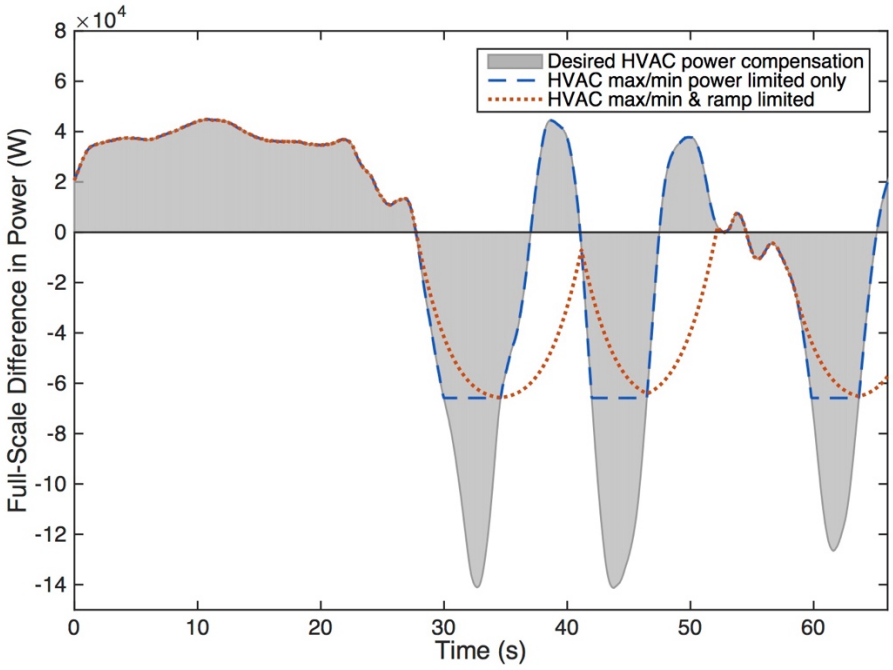

Figure 3.10. Desired power compensation requested from full-scale HVAC systems with and without speed clamps and ramp limiting.

Ramp-rate acoustic changes when following a filtered profile as in Figure 3.9 can be decomposed into changes in amplitude and changes in frequency. These dominant frequencies can originate from motor properties or structural resonances and correspond to different operating regions. Figure 3.11 highlights the recorded sound frequency amplitudes across the audible spectrum when moving from a high-speed "Loud" region to a low speed "Quiet" region. The regions are designated in the top part of the figure by the light (pink) region around 20 s and the darker (green) region around 32 s. The middle depicts the frequency content for comparison of frequency amplitudes. Obviously, louder periods will contain greater broadband frequency content, but to focus on just the pitch changes, the bottom portion of Figure 3.11 normalizes the peak frequency amplitudes. This isolates the pitches from changes in amplitude. The encircled regions indicate dominant frequencies that arise or become noticeably absent relative to baseline operation. Therefore, while not an explicit constraint, frequency changes should not be ignored as they will likely contribute to the conspicuousness of speed changes.

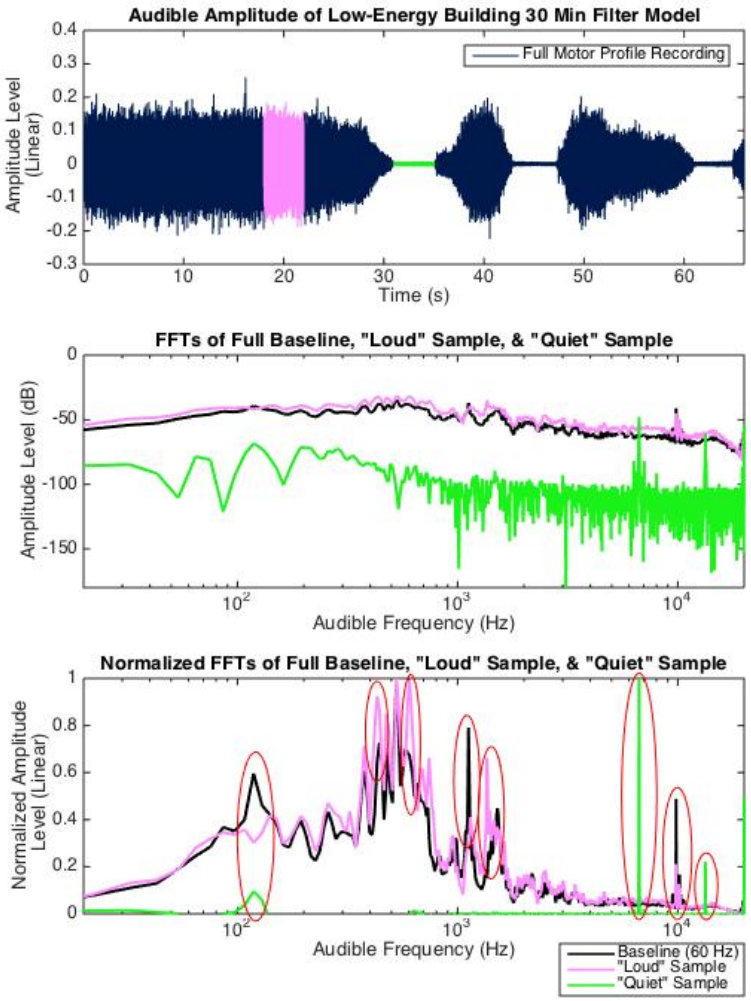

Figure 3.11. Sound amplitudes across audible frequency spectrum for the baseline, “Loud” sample, and “Quiet” sample.

3.4. Effectiveness of dynamic HVAC compensation

Depending on the PV capacity installed and the relative size of the building load, the capability of dynamic load compensation will differ. Table 3.1 summarizes capabilities for different building types with average solar power installations ranging from 25% to 100% of average building load. Figure 3.12 depicts the same data in graphical form. To understand the origins of these results, a 1 min sample of this potential power compensation was depicted in gray in Section 3.3.2, Figure 3.10. The filtering capabilities of Table 3.1 for maximum and minimum limitations were found by integrating the area under the dashed (blue) curves and solid (light gray) curves and then finding the ratio between the two. The ramp-limited case is more complicated because, as observed in Figure 3.10, the power consumption represented by the dotted (orange) curve is effectively time-delayed relative to the ideal filter. Table 3.1 confirms this unfortunate side effect with ramp-limited filtering percentages that are strictly less than or equal to the capacity limited case.

Table 3.1. Filtering Capability Percentage Compared to Ideal HVAC Filter

Average Solar Capacity (as % of total load)		Upper Filter Limit (period in min)	Max/Min Limited Filtering Capacity	Ramp-Rate Limited Filtering Capacity	Acoustic Amplitude & Ramp-Rate Limited Filtering Capability
	100	1	73.20%	57.90%	47.00%
		5	70.70%	65.40%	44.50%
		15	66.90%	63.90%	39.90%
		30	65.20%	62.90%	37.70%
	50	1	89.50%	74.20%	62.20%
		5	85.80%	79.40%	61.00%
		15	84.70%	81.10%	56.00%
		30	83.50%	80.80%	54.40%
	25	1	98.80%	92.30%	80.30%
		5	96.60%	91.70%	77.70%
		15	95.90%	93.00%	75.40%
		30	95.70%	93.40%	73.70%

There are a few general take-away points from Table 3.1 or Figure 3.12. Most obviously, the filtering capability of HVAC systems approaches the ideal case (100% desired filtering) as the average power of a solar installation decreases in relative size to the average HVAC power. Decreasing or eliminating limitations such as ramp rate and acoustic amplitude of course permits increased capability as well. More subtly, while the ideal HVAC filter increases in effectiveness with shorter period filters (less energy to filter), realistic implementations including ramp limiting controls perform more ideally for longer filter cut-off periods (30 or 15 min) due to the slower dynamics. Fortunately, this coincides with utility aspirations of more constant power over periods of 15 or more minutes [20].

In the scenarios studied, not all desired variation could be absorbed through dynamic HVAC compensation. However, in buildings with occupancy sensors, less stringent limitations could be set in unoccupied rooms or zones, enabling increased energy storage potential. Dynamic load compensation might also be sufficient if some PV variation could be eliminated at the start, as will be discussed in Chapter 4. Otherwise, the missed or unfiltered energy must be absorbed by other energy storage mechanisms, as mentioned in Section 1.4.1.

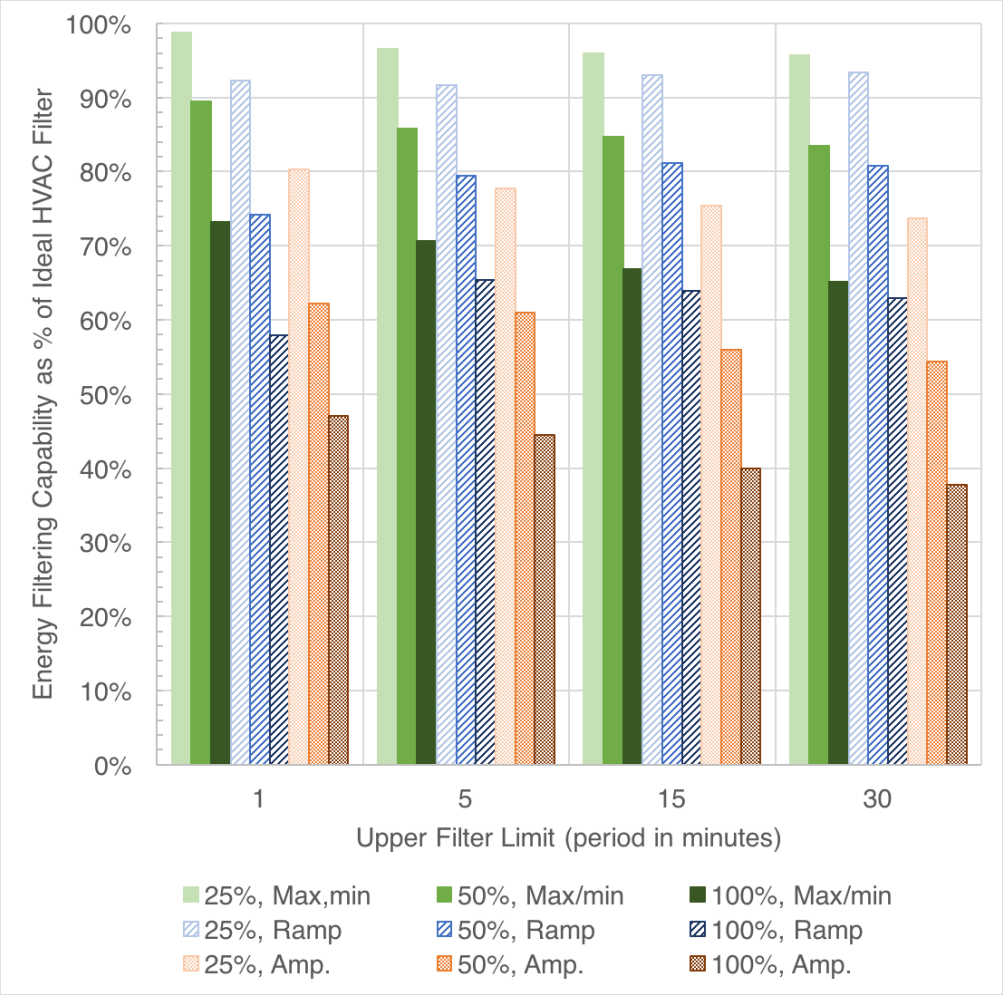

Figure 3.12. Graphical representation of Table 3.1.

3.4.1. Reduced battery storage requirement

Implementing dynamic load compensation should require no more than an outer control loop built on top of existing thermostatic controls and variable speed drives, which are becoming the norm in new commercial buildings. Therefore, the cost of implementation is almost certain to be lower than the additional battery storage that it is meant to offset. Results from a ten-day sample suggest that a battery storage unit could be downgraded in size by at least 25% with the dynamic HVAC compensation strategy discussed [39]. The benefits of dynamic load compensation are visibly present as well. One sample day is provided in Figure 3.13 and indicates the reduction in battery demand (filled-in regions) when dynamic HVAC load compensation is implemented vs. the baseline case of raw solar power (middle vs. top). Figure 3.13 also includes an additional scenario where the principle of dynamic load compensation is extended to a large water reservoir used for chilled beam cooling (bottom). In this case, battery storage requirements are nearly eliminated.

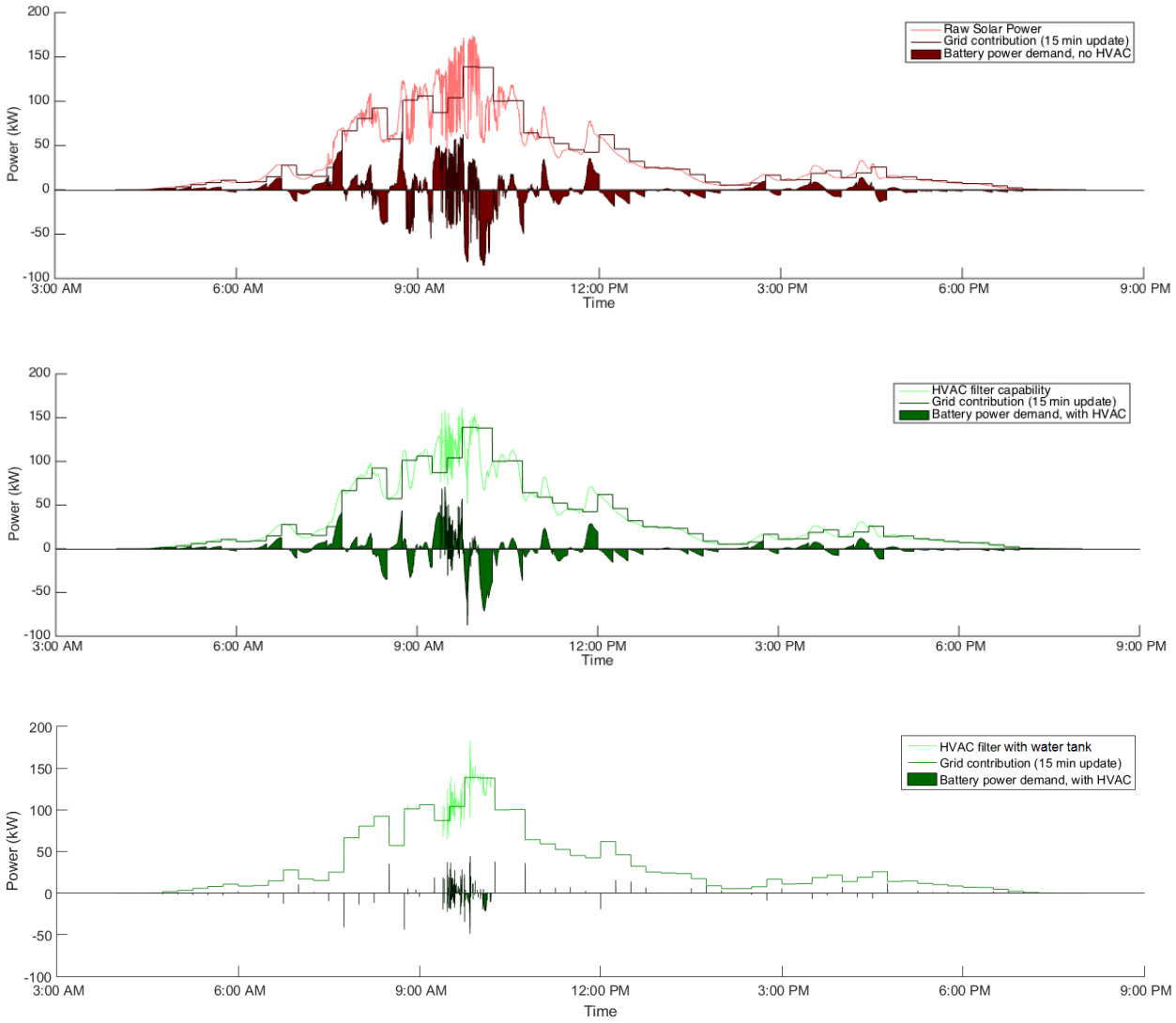

Figure 3.13. Grid and battery energy contribution for: raw solar profile (top), filtered solar profile using just HVAC (middle), and filtered solar profile with HVAC and water tank acting as dynamic load compensators (bottom).

Another benefit of dynamic load compensation is the reduction of energy entering and exiting the battery, degrading battery lifetime. Compared to the baseline case, HVAC filtering can reduce energy cycling by more than 25% for an overcast day, and nearly eliminate energy cycling when combined with dynamic load compensation of a very large water tank. While excess thermal losses associated with increased temperature gradients have not yet been considered, there is potential for significant energy savings from reduced power electronic losses and battery cycling inefficiencies.

4. PV Operating Reserve Curtailment

PV operating reserve curtailment can eliminate short-term solar power variability by partially controlling the power production of a PV panel or system. In other words, the technique enables more predictable power output by attempting to supply certain power set-points rather than simply tracking the natural dynamics. PV operating reserve curtailment has been shown to effectively and economically prevent the production of significant variability at the panel level [40]. This chapter restates many of the arguments and findings previously published in [40]. As an overview, this chapter focuses on what is meant by dynamic operating reserve curtailment, the electrical benefits that PV systems can provide, the economic argument for why some level of reserve-based curtailment makes sense, and a few different variability and optimality metrics.

4.1. Operating reserve curtailment scheme

Both curtailment and reserve can have multiple definitions depending upon the application. For this thesis, curtailment means operation of a PV panel at some power set-point below its MPP while reserve is the power (or percentage of power) available on top of the commanded set-point. Dynamic operating reserve curtailment is the combination of these two in a time-varying environment. To clarify, operating reserve curtailment is not equivalent to continuous operation at a nominal fraction of MPP output. Instead, a nominal fraction is set, and then a low-pass filter control or other slow strategy is used to calculate a slow-changing set-point or power target. In this way, a PV system actively offsets some of its own variability. The set-points could also come from historical solar data, weather forecasts, generic output profiles, 15 min constant or first-order grid commands, or combinations of these or other inputs.

To illustrate the concept, a PV system employing operating reserve curtailment with a low-pass filter was simulated and analyzed on the same June 15th, 2003 data used throughout Chapter 3. Much like Section 2.2.3, variations in the MPP power (not current or voltage) were of concern. A subset of MPP power data and the calculated reserve powers (nominal 10% held in reserve) is seen as the solid, jagged curves (gray) near the top of Figure 4.1. The heavy, dotted and dash-dotted curves (in red) are calculated from a 1st-order low-pass Butterworth filter applied to the peak and reserve power curves. Since these filters are causal and slow-changing, a high-probability estimate of the next moment's power target could be found through extrapolation methods based on past data. Relative to the MPP filtered set-point, excesses or shortages imposed upon the grid are called fluctuations and is represented as the jagged, dashed curve near the axis (pink) in Figure 4.1. If pure curtailment is permitted, then all instances of excess power can be eliminated. Additionally, if the reserve set-point is

used instead of the MPP set-point, then power short-falls can be partially or completely supplied thanks to the available power reserve. Such a scenario with 10% reserve can be described as the heavier, solid, mostly flat curve near zero (purple) in Figure 4.1. Note that a majority of the time, the power target could be achieved (fluctuation from set-points = 0) and that residual deviations are reduced in magnitude compared to the MPP case.

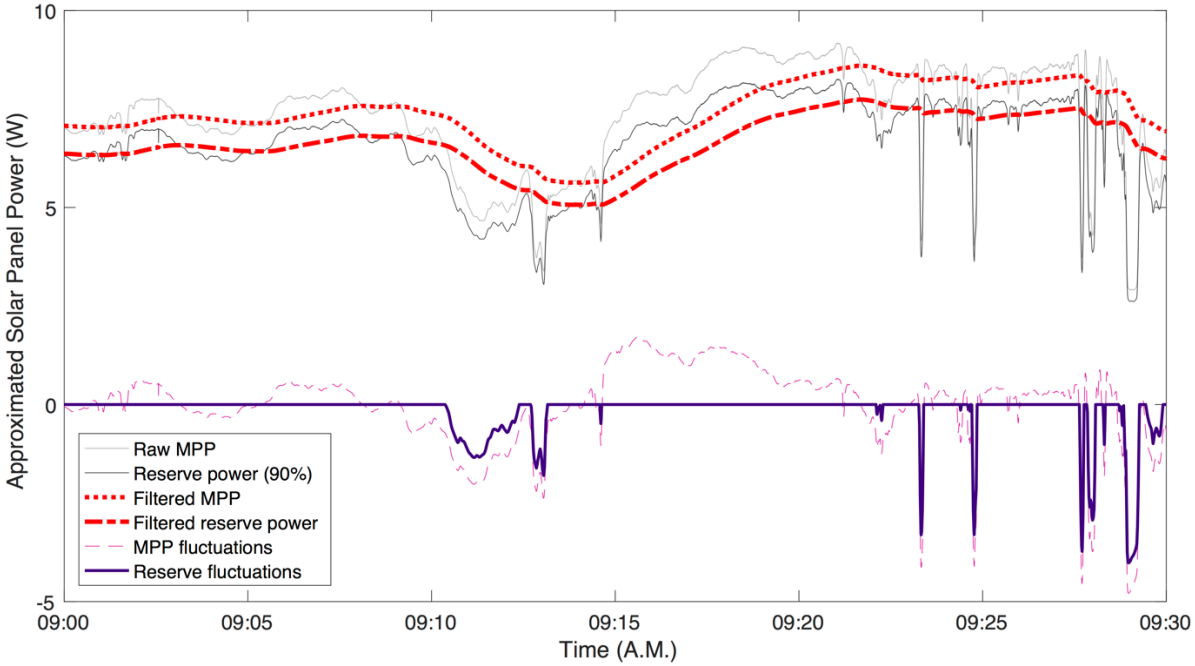

Figure 4.1. MPP PV power available, reserve power, associated "filtered" power targets, and remaining fluctuations imposed upon the grid.

A modified incremental conductance algorithm was designed and simulated that would operate at the power target when possible and maximize power output when experiencing a shortage. Chapter 5 contains details of the project, the algorithm, and simulated results.

4.2. PV systems as a grid resource

When photovoltaic technology was new and inherently expensive, it made sense to continuously operate at peak capacity to maximize energy output. Unfortunately, this meant that solar installations behaved like “negative load” grid connections – introducing stochastic variability, producing unregulated power output, and potentially degrading system dynamic performance [41]. As the cost of PV continues to decrease, however, it may be time to transition from PV as a liability to PV as a grid resource. When it comes to traditional spinning generation, active grid support, implying dynamic control, is essential for full-function supply-side resources. Without similar controls for PV systems, models of PV generation (as

in [42]) typically add fossil fuel reserve capacity to help offset intermittency. However, we do not have to operate PV this way. It can not only offset some of its own variability, but also, together with an "active" grid-ready inverter, it can actually offer grid support beyond what conventional generation provides.

Not including energy storage, some examples of active grid support include:

- Voltage support – Reactive power capability to help regulate local voltage.
- Frequency support, including regulation up and down – Real power adjustment to maintain fixed frequency.
- Operating reserves – Additional capacity that can be connected when required.
- Ramp rate capability – Track expected load ramping at near arbitrary rates.
- Stability maintenance – Rapidly respond to faults, line removals or insertions, or large instantaneous load changes.

The inverters for grid connection in many PV systems operate at unity power factor and maximum power capacity at all times, and therefore do not provide *any* of these active support capabilities. The situation is changing rapidly in Europe, however, as requirements for active inverters move toward standardization [43]. Reactive power and voltage support are feasible in these designs, and the implementation of reserve could mean available inverter capacity even during times of peak power production. Low-voltage ridethrough, requiring continued operation through an external fault, is emerging in PV systems. Frequency support and other regulation requirements tend to be one-sided, requiring power reduction during over-frequency conditions or power curtailment in some situations [30]. Operating reserve curtailment could expand this capability to include some level of power increase during under-frequency conditions. Broader active grid support is typically associated with storage, but dynamic controls for active grid functions are possible even with small inverters [44].

4.3. Economic justification of PV curtailment

All of the potential benefits of PV curtailment with operating reserve must be made economically competitive against alternative solutions. This section argues that some reserve capacity *does* make economic sense given grid support as an inherent requirement of supply-side resources.

For some tangible metrics, consider the cost of PV energy to be about $0.05/kWh [45] and the cost of conventional spinning reserve to be $0.0058/kWh [42]. Photovoltaic (PV) energy systems have quoted installation costs at or below US$2 per peak watt across scales from residential [46] to utility [47]. In

systems with 25 year warranties, this means that electricity is produced below $0.05/kWh at this installed cost. As a side note, this approaches *cost parity*, at which PV energy production costs are comparable to those from other fuels measured at distribution points in the grid [45]. The cost of operating reserves has been explored in depth by NREL [42] and averages about $5.80/MWh, or the $0.0058/kWh figure. Conventional PV practice treats any energy sacrificed as having an opportunity cost of $0.05/kWh; however, this neglects the cost of regulation which either must be supplied by traditional generation or battery storage. Battery storage, for comparison, has target costs of $250/kWh, installed [14]. Assuming linear degradation, more than 40,000 equivalent cycles would be necessary to be cost competitive with spinning reserves. This is unlikely with modern battery technology.

Consider instead the scenario in which the value of a PV system as a generation resource is maximized rather than just the energy production. Say that, on average, 10% of available power is set aside for grid support. Therefore, the cost of this reserve would be 10% of the overall cost of energy, with the caveat that the remaining energy is now about 10% more expensive. After all, for the same installed system, 10% reserve means that you would only be receiving 90% as much energy as without reserve. Mathematically, the cost of reserve is calculated to be

$$\boldsymbol{C_r = \frac{P_{solar}}{(1-\chi)} \cdot \chi} \tag{4.1}$$

where the cost of solar energy is labeled as P_{solar} and the reserve fraction as χ. We see in Figure 4.2 the cost of PV operating reserve curtailment plotted over various amounts of reserve. The circles (blue) curve represents the approximate cost of modern PV technology, as discussed, while the triangles (orange) curve represents a hypothetical future cost as PV continues to get cheaper. The solid (yellow) line represents the cost of spinning reserve, below which PV reserve has a cost advantage.

As would be expected from (4.1), increasing reserve corresponds to significantly increased cost. This is because larger amounts of reserve constitute larger fractions of the baseline PV cost and effectively cause the remaining energy to be more expensive. In contrast, small percentages of reserve cost very little. This means that for *any* PV price level, including the very pessimistic gray (squares) cost curve in Figure 4.2, *some* percentage of reserve is cheaper than conventional reserve resources. Curtailment cost issues erode as PV installed costs continue to fall and as PV inverters become responsible for more than just energy conversion. In this analysis, no economic value was attributed to potential PV inverter grid support capabilities, though these could certainly defray some reserve costs.

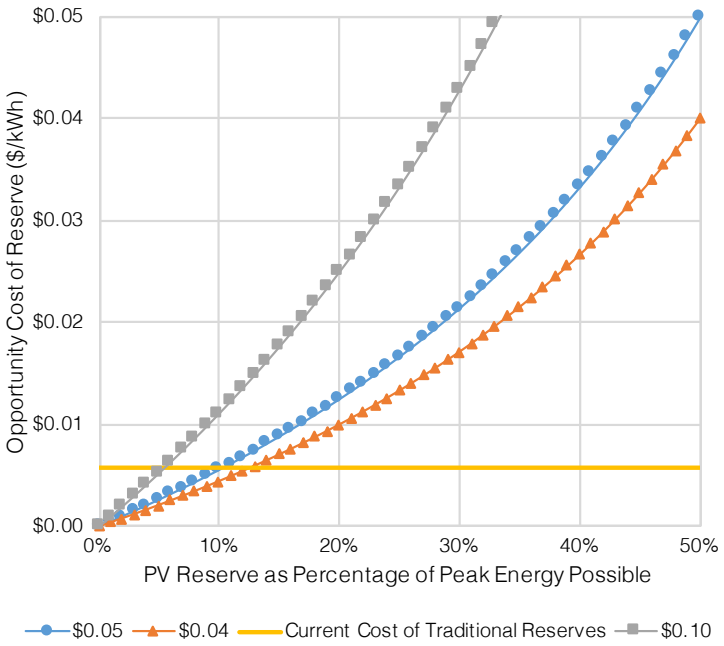

Figure 4.2. Opportunity cost of reserve for different prices of solar as compared to conventional reserves.

4.4. Measures of variability and optimality

PV variability can be defined in a number of different ways. Section 4.1 refers to variability as the deviation from the low-pass filtered peak power profile. This can be defined in at least two different ways - either the maximum absolute difference or the integral of power differences. This section presents how the operating reserve curtailment scheme reduces variability in both metrics. Additionally, while the focus of this thesis is to reduce variability, the value of renewable energy is not to be ignored, so one measure of optimality is presented that tries to maximize energy production while minimizing variability imposed upon the grid.

Let us first consider variability as defined by the peak difference between the power available and the output power set point. Allowing for curtailment means that only negative variability (power below the set point that cannot be supplied) will persist, because positive variability would represent an excess that could be curtailed to meet the set point. Figure 4.3 shows comparative operation on a day with substantial cloud cover variation and intermittency. In the left plot, actual solar production (scaled to an arbitrary power peak) is shown as the light trace, and the desired output based on a low-pass filter inverter set point, but no reserve, is shown as the dark trace. All negative variability is imposed directly on the grid, and as such, the maximum, traditional (spinning) operating reserve would be the ratio of the negative peak in variability to the positive peak in the solar data, in this case about 5/11.5 or 43%. In the right plot, the same control is employed with a nominal 85% operating set point. This allows for some

negative variability to be reduced by utilizing some reserve power capability, and thus there is a substantial reduction in variability imposed on the grid. The operating reserve requirement drops to 3.6/11.5 or 31%; the drop is not quite a 1:1 reduction (15% PV for 12% conventional), but it is still substantial.

The alternative, integral definition of variability is perhaps better suited to battery storage metrics rather than spinning reserves as it represents watt-hours of energy storage rather than just watts. A claimed "reduction in variability" would be the difference between the base case and the reserve case fluctuation integral. This corresponds to the difference taken between the integrals of the bottom (purple) curves in Figure 4.3.

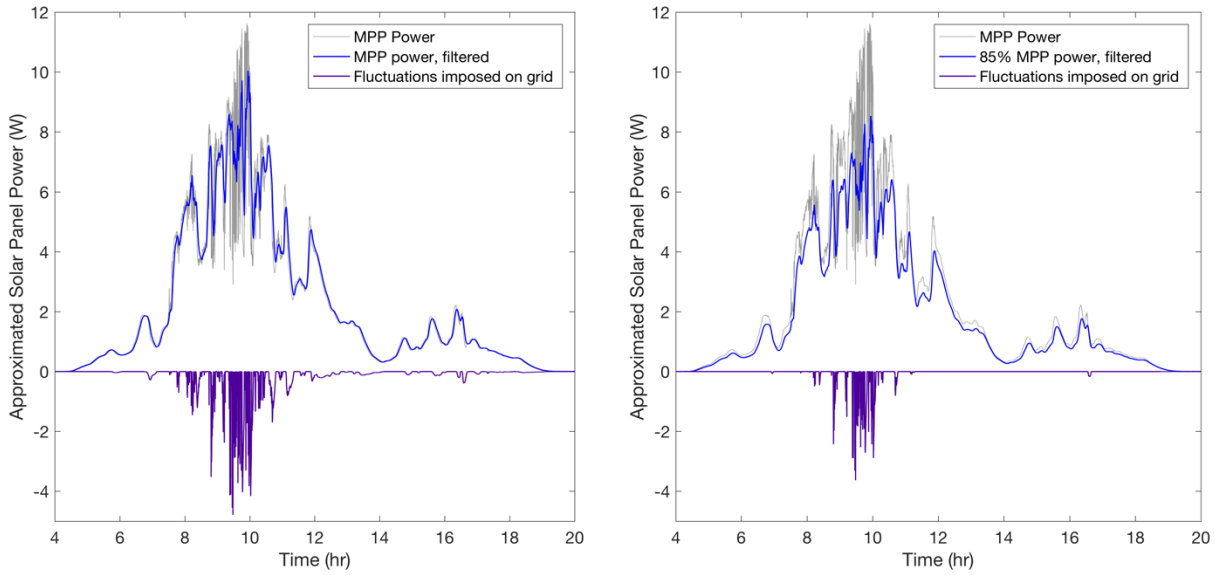

Figure 4.3. Variability mitigation over a day with substantial solar intermittency (June 15th, 2013). Left plot: no reserve capability. Right plot: nominal 15% reserve.

The integral definition of variability was used to calculate the optimal PV reserve percentage. Generally speaking, increasing the nominal reserve will reduce variability but increase energy sacrifice. Much like the absolute variability related to spinning reserve reductions, the integral variability does not trade off with energy sacrifice in a 1:1 manner. Instead, it is nonlinear and depends upon the "type" of day as it pertains to various amounts of cloud cover. Figure 4.4 shows the reduction ratio vs. the nominal curtailment level for the same three days as Figure 2.6. Each type of day experiences a level of reserve above which increased reserve has diminishing returns. The peak of this curve represents one measure of optimality as the marginal benefit of increased reserve is maximized at this point. This point of optimal operation typically supports the overall cost-benefit analysis, too.

According to Figure 4.2, modern day systems operating with 0-10% reserve correspond to direct energy reduction costs that are lower than reduced operating reserve costs in the power grid. For example, in Figure 4.4 an optimal trade-off is observed at about 8% reserve for the overcast day. Given a $2/W PV system, a curtailment of 8% translates to effective operating reserves costing $174/kW and $4.35/MWh using an approach similar to (4.1). These values are substantially lower than existing grid reserve methods, and for clear and overcast days this is likely to be the case. Days with intermittent cloud cover pose a larger obstacle to variability reduction so the optimal energy vs. variability point may lie to the right of the cross-over cost in Figure 4.2 and may thus be cost limited and not quite ideal.

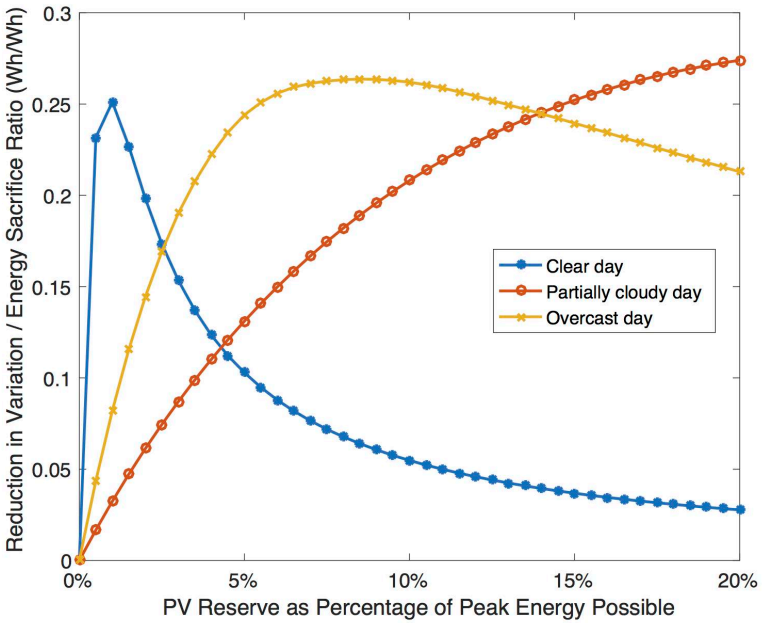

Figure 4.4. Cost-benefit curves for finding optimal reserve percentage.

The optimality curves of Figure 4.4 indicate that the best reserve level should adapt to conditions. Though outside the scope of this thesis, a hybrid approach of low-pass filtering and weather forecasting may lead to improved energy capture and variability reduction. For example, weather forecasts for partial or full days could be distributed to control algorithms through internet connectivity and set recommended reserve capacity based on predicted cloud cover type and quantity. Then, the low-pass Butterworth filter would use the updated curtailment level when determining power set-points. Alternatively, reserve percentages could be dynamically increased and decreased based on the perceived volatility, relaxing during periods of clear sky and slow changes and increasing during periods of partial cloud cover.

5. Implementation analysis

The proof of concept Simulink model presented here demonstrates the successful modification of an incremental conductance maximum power point tracking (MPPT) algorithm to achieve the desired, arbitrary power output. More specifically, the model sets a target power output based on "filtered" historical, curtailed solar data and then operates at varying levels of curtailment to best match the desired output. This capability is coined desired power point tracking (DPPT).

As a broad overview, Section 5.1 reviews the conventional operation of the incremental conductance algorithm and introduces the modification used to operate at points away from the MPP. Section 5.2 then builds up the model piece by piece, beginning with a simple control loop and evolving into the final control system with cross comparisons and verifications between versions along the way. The final output to some sample data may be found at the conclusion of this section. Section 5.3 then provides some brief economic justification and an alternative perspective for why trading uncertainty for energy production might make sense.

5.1. Incremental conductance – a review

The proposed implementation of power curtailment is based on an incremental conductance MPPT algorithm, so it is important to understand its typical operation before proceeding. In addition, a high level description of how DPPT adapts this algorithm is presented.

5.1.1. Conventional algorithm

Incremental conductance relies upon measurements being taken at discrete instances in time. At each time step the algorithm compares the latest voltage and current measurements to the prior measurements and then calculates the difference to obtain ΔV and ΔI. By comparing the instantaneous conductance, I/V, to the negative of the discrete change in conductance, -ΔI/ΔV, a decision can be made to either increase or decrease the operating voltage set point. The derivation of the incremental conductance relationship is as follows: The slope is 0 at peak power on the power vs. operating voltage curve (Figure 5.1). This MPP is indicated in the figure by the circles atop each irradiance curve. Put simply,

$$\frac{dP}{dV} = 0 \tag{6.1}$$

at the MPP. Next, we expand out the power P into its voltage and current components and evaluate the derivative using the product rule.

$$\frac{dP}{dV} = \frac{d(I \cdot V)}{dV} = \frac{dI}{dV}V + \frac{dV}{dV}I = \frac{dI}{dV}V + I = 0 \tag{6.2}$$

We approximate that for rapid sampling (faster than the dynamics found in the solar data) we can replace the instantaneous derivative with a ratio of discretized differences.

$$\frac{dI}{dV} \approx \frac{\Delta I}{\Delta V} \tag{6.3}$$

Implementing this approximation and simplifying the expression into two conductance terms, we have

$$\frac{\Delta I}{\Delta V} + \frac{I}{V} = 0 \rightarrow \frac{\Delta I}{\Delta V} = -\frac{I}{V} \tag{6.4}$$

where the term on the left of the equals sign is called the incremental conductance and the term on the right is the instantaneous conductance.

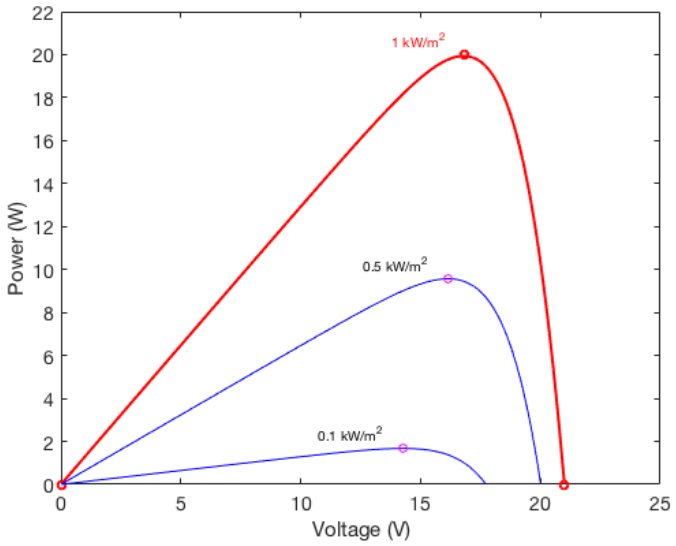

Figure 5.1. Power vs. operating voltage curves for three different irradiance levels.

The final step for the incremental conductance algorithm is to either increment or decrement the operating voltage (x-axis in Figure 5.1). Considering that dP/dV is greater than 0 to the left of the MPP we can use the final expression in (6.2) and (6.4) to infer that when the incremental conductance is greater than the negative of instantaneous conductance, the operating point is likewise to the left of the MPP and that the voltage set point should be incremented. The complimentary state and actions for dP/dV less than 0 likewise hold.

5.1.2. Modified algorithm

The conventional algorithm presented in the previous subsection is designed to operate at peak power, but for DPPT, it is most often the case that the desired operating point will not be the MPP. It was therefore necessary to generalize the incremental conductance algorithm to accept target operating

points below the MPP and corresponding non-zero slopes. Mathematically, rather than searching for the zero slope point as in (6.1), we are now searching for where

$$\frac{dP}{dV} = S \tag{6.5}$$

where S is the variable for slope. Following the same procedure as in Section 5.1.1, we obtain

$$\frac{\Delta I}{\Delta V} = \frac{S - I}{V} \tag{6.6}$$

at our desired operating point. Just as before, if the incremental conductance is greater than the negative of this new, modified, instantaneous conductance, then the operating point is to the left of the DPP and thus the voltage set point should be incremented. The complimentary state and actions again hold.

Figure 5.2 represents such a scenario where the power demanded is 90% of peak power for that irradiance. The target power and associated slope are indicated by the green dot and straight line that passes through it. Note that only the non-shaded region to the right of each MPP is utilized. Even though there are two points at which output power equals the desired fraction of peak power, the slope to the left of the MPP is largely constant, which leads to poor conditioning of the look-up values to be discussed in Section 5.2.4.

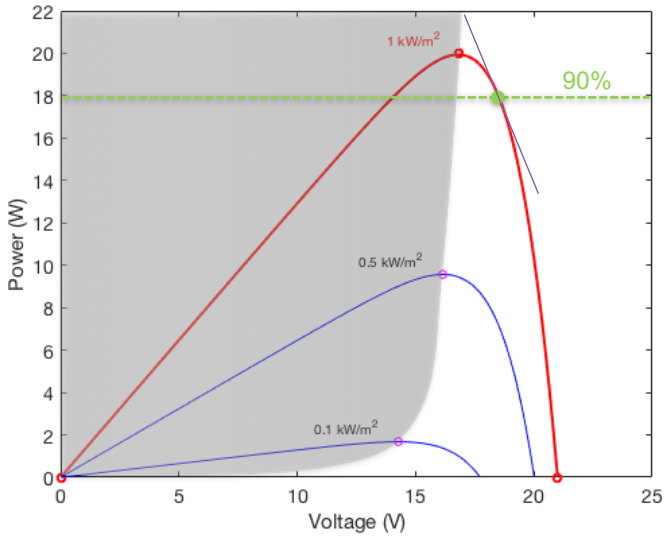

Figure 5.2. Useful region of power vs. operating voltage curves (non-gray section) with a new target power (green dot) and associated power vs. voltage slope indicated on the peak irradiance curve.

5.2. Modeling procedure and verification

To ensure accuracy of the final result, the simulation was built in multiple stages with each successive stage adding either a new subsystem or a simplifying approximation. Additionally, the simulation utilized

PV data from the finalized data set presented in Chapter 2 to model the response to real-life PV power profiles.

5.2.1. Stage 1: Base case

The base case consisted of a classical incremental conductance algorithm wrapped around a boost converter. The boost converter was implemented with a model MOSFET and diode as well as PWM generator built from a triangle waveform generator, the output from the control loop, and a comparator. The output of the boost converter was connected to a fixed-voltage bus of 95.2 V. Such an arbitrary value is the result of a scaling approximation. Initial model plans were for a more-typical 235 W panel with 30 V_{MPP} to be connected through the boost converter to an ideal voltage-sourced inverter as in Figure 5.3. The configuration might resemble a typical microinverter that connects a single solar panel directly to the ac electric grid. In order to output a 120 V_{RMS} waveform to the grid, the boost converter would need to supply a 170 V dc bus (for an ideal inverter). In order to transform the panel parameters from Chapter 2 (20 W, 16.8 V_{MPP}) into those for the 235 W panel desired, a linear scaling approach was taken, much like Section 3.2.2. That is, a converter boosting 30 V to 170 V was assumed to have linearly proportional dynamic properties to one boosting 16.8 V to 95.2 V.

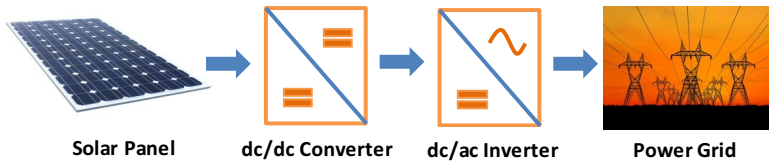

Figure 5.3. Block diagram illustrating the envisioned implementation of a MPPT boost converter as part of a microinverter.

In order to permit numerical integration without a singular solution, Simulink required a small resistance in series with either the voltage source or output capacitor. Consequently, an 8.13×10^{-4} p.u. resistor was inserted in series with the infinite bus. The resistor was placed here instead of in series with the capacitor to avoid excess ESR-related voltage jumps at the output. The selected placement conveniently resembles line resistance that would be likely encountered if implemented in real life.

5.2.2. Stage 2: Average circuit model

Simulating just 0.1 s of model time in the base case took considerable computational power and time - probably over 100 s on a 2.4 GHz dual core processor. Significant solar variation caused by clouds occurs over a period of a few seconds to minutes, so the simulation had to be drastically simplified if it were to provide any meaningful results in time. To this end, the switching circuit was replaced with an average

circuit model to observe the response of the converter on time scales much longer than a few switching periods.

Modifications from the switching model included switch replacement and an increase in output capacitance. The diode in the base model was replaced by a dependent current source valued at $(1 - D) \cdot I_L$ where I_L is the average inductor current; the MOSFET was replaced by a dependent voltage source valued at $(1 - D) \cdot V_{out}$ where D is the commanded duty ratio; and the output capacitance was increased significantly. Since the average model has a tendency to exaggerate oscillations, the increased capacitor size dampens the response to create similar output power responses to duty ratio perturbations. The output power waveforms from the base case with switching and the average case are largely consistent (Figure 5.4). Differences include a slight phase shift due to the effect of local averaging, and larger steady-state ripple in the base case due to the switching ripple.

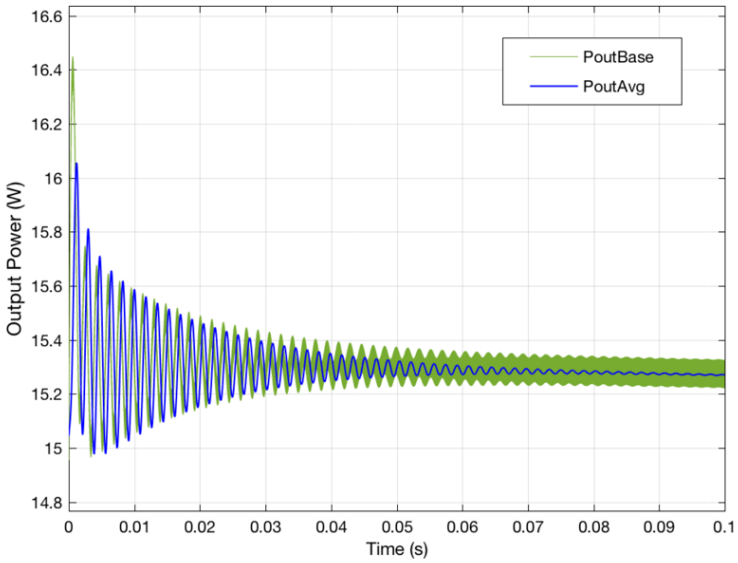

Figure 5.4. Power output response to start-up disturbance.

5.2.3. Stage 3: Constant curtailment

Before implementing any advanced control, it was important to ensure that the modeled boost converter could properly operate at a desired level of curtailment. In this stage, a fixed fraction of reserve was set, namely 10%. Figure 5.5 shows the power output of the converter with 10% reserve in green. Maximum possible power from the panel is shown in orange and the desired output power of 90% peak power is shown in blue for comparison with actual power output.

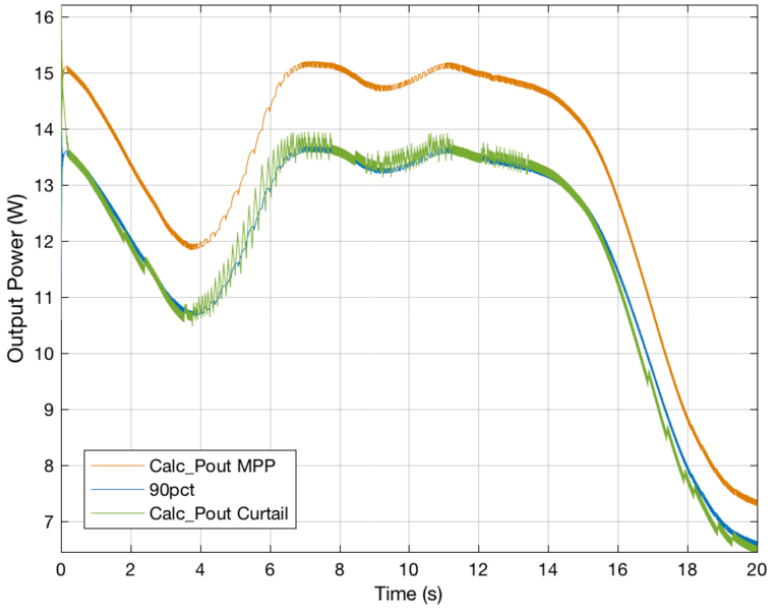

Figure 5.5. Power output with a fixed curtailment (reserve) command relative to ideal case.

The modeled converter output closely tracks the ideal 90% peak power curve with two distinct feature types of note. The first is small, intermittent step changes that typically bring the output closer to the desired level. While not confirmed, these are likely due to the discrete changes in look-up table values. As the algorithm transitions from one breakpoint to another, it is possible that irregularities in the slope value along the x- or power-axis of Figure 5.6 could cause some jagged behavior. The other feature is triangular oscillation about the desired operating point, most notably where increases in power output are desired. This near instability is likely a result of the boost converter's naturally occurring right half plane zero in combination with control actions that are delayed by 0.01 s from the measurements taken and a limited set-point voltage step rate. When more power is desired, the converter output voltage will initially drop before rising again. However, if the control measures this decrease, then 0.01 s later it will demand that the next step be an increase and only add to potential overshoot.

5.2.4. Look-up table creation

One of the downsides to the proposed algorithm is that you need advanced knowledge of the power vs voltage slope for each level of curtailment desired. Unfortunately, the desired slope also changes with irradiance for a given curtailment level. Therefore, a two-dimensional look-up table was used to indicate an approximate slope for a given curtailment level and peak power (related to level of irradiance). Figure 5.6 is a graphical representation of the look-up table where the x and y axes represent "inputs" and the associated z value "output" at those coordinates represents the slope dP/dV for those conditions.

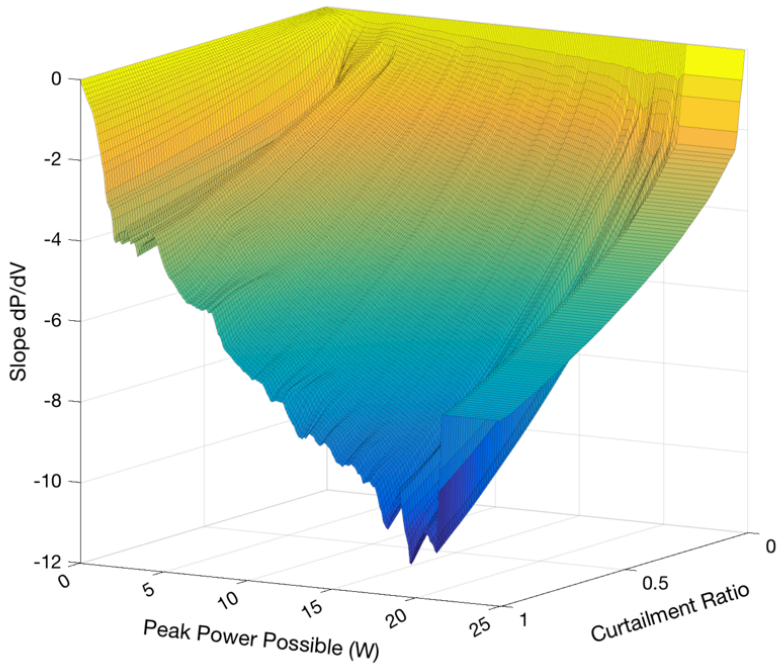

Figure 5.6. Look-up table in graphical form.

Photovoltaic current vs. voltage (I-V) curves also have a temperature dependence, but these effects will be secondary in significance and would require a 3-D look-up table, so temperature dependence was ignored in this analysis. Creation of this look-up table was still complicated, however, and involved the following procedure:

1. Extracting raw, slow meter, I-V sweep data (as discussed in Section 2.1) for August 1st, 2013.
2. Grouping well-behaved I-V sweeps (as defined in Section 2.3.4) into 0.1 W resolution bins based on the peak power of each.
3. Calculating the mean I-V sweep for each bin.
4. Deleting values of P-V pairs to the left of the MPP.
5. Performing "localized moving average" operations to smooth the P-V data to be monotonically decreasing.
6. Calculating discrete derivatives with a centralized difference approximation

$$\frac{\boldsymbol{P_{i+1} - P_i}}{\boldsymbol{V_{i+1} - V_i}} \approx \mathbf{S}_{\mathbf{i+\frac{1}{2}}} \tag{6.7}$$

   in order to create a slope vs voltage or S-V curve.
7. Repeating the "localized moving average" where needed (on non-monotonically decreasing derivative curves).
8. Using linear interpolation on the P-V curve to calculate approximate voltage associated with each discretized curtailment level between 0% and 99% of peak power.

9. Correlating each interpolated voltage with a slope value, again using linear interpolation.
10. Repeating this process (steps 2-9) for each peak power range or “bin”.
11. Running a 5-element-wide window moving average across the peak power possible values for constant curtailment ratio to try and smooth out the rather jagged output data surface.

Once all of the above steps were performed, the output yielded Figure 5.6, which is the same data used for the look-up table in the DPPT algorithm.

5.2.5. Butterworth calculation

Once the constant curtailment was functional, most any piecewise continuous power output sequence could be commanded. In this study, the same low-pass Butterworth filter was implemented as in Chapters 3 and 4 except with a low-pass cutoff of (1/60) Hz (or slower than 1 min). Once achieved, this target power output would possess much slower dynamics than the raw solar data, decreasing the uncertainty associated with solar power from a utility perspective. With this expected operating point, any time that available power is greater than commanded power the solar power can be curtailed to produce the expected power output. The purple curve in Figure 5.7 represents power commitment or command that cannot be met with this strategy because there is no headroom/reserve during those times. The integral of these shortcomings is defined to be the remaining variability, and must be met with additional energy storage or reserves if the Butterworth-filtered commitment is to be met.

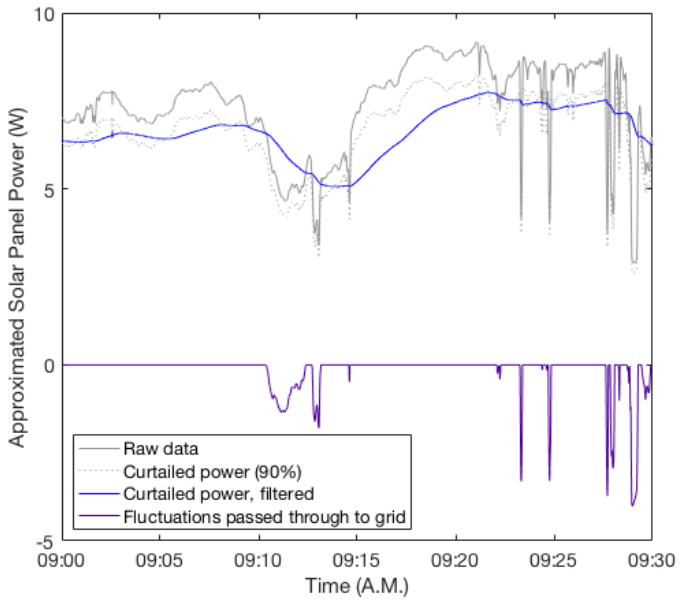

Figure 5.7. Raw solar data together with filtered, curtailed power demanded, and power lacking curves.

5.2.6. Results

The final step in this model creation was to implement the Butterworth filter into the control loop. The filter took as input raw data multiplied by one minus the nominal reserve or 0.90 in this case. The output was used to calculate the next curtailment percentage command, and dividing the current panel power by the filter output provided the needed estimate of peak power available at that instant. Figure 5.8 illustrates a sample of the final output in which the darkest curve (black) represents the MPP at all times, the medium darkness curve (blue) is the nominal 90% value for the case where 10% reserve is desired, and the smooth, dashed curve (magenta) is a first-order, low-pass, Butterworth filter with cut-off frequency of (1/60) Hz. The light curve (green) represents the modeled output of the DPPT algorithm, which as desired, tracks the magenta Butterworth curve whenever possible, and maximizes power output (tracks orange curve) whenever insufficient power is available. Again, there is notable, triangular oscillation about the filtered power set point (Figure 5.8) though this virtually disappears when limited by the peak power.

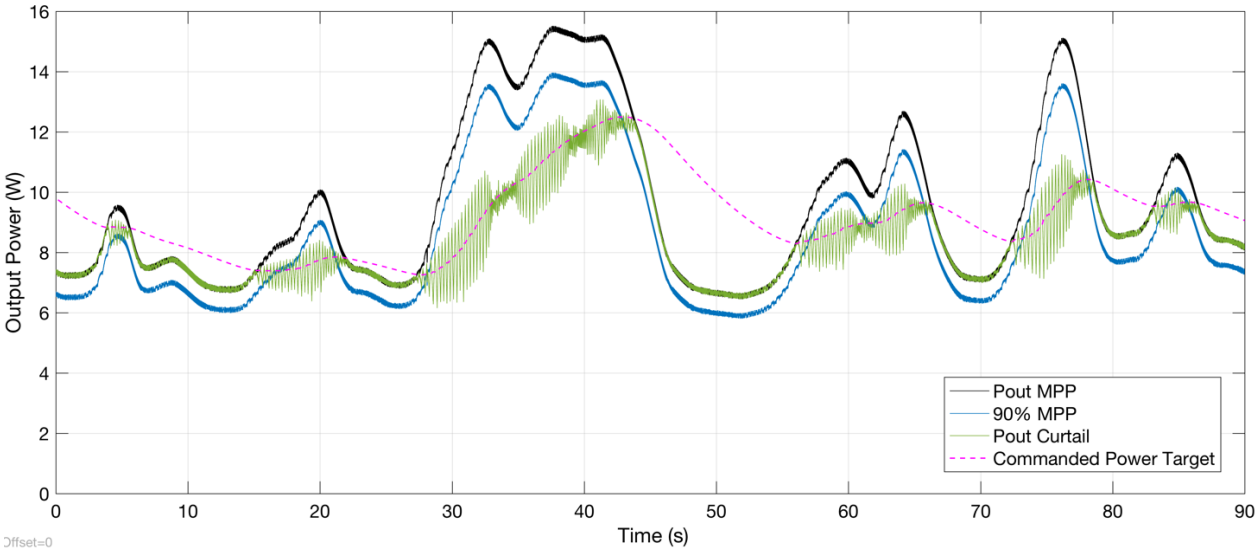

Figure 5.8. Actual output of DPPT model compared to commanded power set-point with raw MPP data and 10% reserve curve for reference.

5.3. Economic justification for implementation

Solar power "reserve" can certainly lower the cost of battery storage necessary to meet power commitments, but the question is if the opportunity cost of the reserve is greater than the battery cost being offset. To investigate this question, two scenarios were compared: (1) MPP solar power is output at all times, and sufficient battery capacity is required to absorb all peaks and supply for all valleys relative to the filtered MPP output. (2) The filtered power output target is based on a 90% nominal

power output, overhead or reserve power can be utilized when beneficial, and solar energy can be "spilled" when not useful in meeting claimed commitment. The simplifying assumptions are that in both scenarios the batteries are lossless and the filtered power output commitment must be met at all times throughout the day.

For case 1, raw capacity was determined to be the peak cumulative sum of energy either supplied or demanded from the batteries. This is because we would need to absorb any possible variation from the filtered power into the batteries to meet our commitment. Excess energy and energy shortages would offset one another in said summation. Actual battery capacity would have to be ~3.33 times larger than the raw capacity so that the battery would operate between 20% and 80% state of charge (SOC) and so that it could start at 50% SOC to equally handle a potential surplus or deficit of equal magnitude.
For case 2, raw capacity is calculated in a similar manner except that full panel power may be used when convenient and energy can be "spilled" by operating the solar panel off of its MPP. The same multiplier of 3.33 will be used for consistency, though in reality, since reserve energy is very likely to be available throughout the day and shortages are typically brief, much less surplus-energy capacity would be needed and the central SOC might be closer to 70% so that overall battery capacity required could be reduced. Alternatively, battery capacity could remain the same as case 1 and be used for nighttime energy rather than pure regulation capability.

For the purpose of this calculation, a sample day was selected from the raw data set. All power and energy values will be scaled by 1000 to represent a commercial solar installation of 20 kW. While battery degradation is likely nonlinear, battery cycling in this analysis was calculated as the cumulative total of all energy in and out as a fraction of necessary battery capacity. The two scenarios were calculated, and full battery storage (scenario 1) would require 0.399 kWh of storage while the reserve-based method would require only 0.131 kWh. Additionally, the filtering required for the sample day would cycle approximately 140% of the battery capacity and in scenario 2, 3.41 kWh of energy would be sacrificed over the course of the day. Taking, for example, the capacity and cost of a Tesla Powerwall battery [48] we can estimate a per kW cost of battery storage to be

$$\frac{\$\mathbf{3000}}{\mathbf{6.4\ kWh}} = \$\mathbf{468.75/kWh} \tag{6.8}$$

With the rated cycling estimate of 5000 cycles [49] at 1.4 cycles per day, that yields ~9.78 years. Call it 10 years for convenience. The reduced battery storage requirement can save

$$\frac{(\mathbf{0.399 - 0.131})\mathbf{kWh} \times \frac{\$\mathbf{3000}}{\mathbf{6.4\ kWh}}}{\mathbf{10 years}} = \$\mathbf{12.56/yr} \tag{6.9}$$

The energy sacrificed can be viewed in two different ways. If viewed as an operating cost, then every kWh missed has the opportunity cost of the electricity rate of about $0.0999/kWh [50]. Thus, over one year the opportunity cost would be a substantial

$$\frac{\$0.0999}{kWh} \times 3.41 \frac{kWh}{day} \times 365 \frac{days}{yr} = \$124.34/yr \tag{6.10}$$

However, we are reaching a point where solar power can no longer be treated as a negative load without grid stability consequences. If it is to be treated as a traditional generator that must provide regulation capability and abide by its forecast commitment, then a cost calculation paradigm shift is required. The cost of regulation becomes part of the *initial solar installation or investment fixed cost*. At current costs, solar energy is estimated to cost $0.05/kWh [45]. If 10% reserve is assumed, then the cost of the solar energy goes up by 1/(1-10%) or 111% and the reserve will cost 10% of this new cost or

$$10\% \times 111\% \times \frac{\$0.05}{kWh} = \frac{\$0.00556}{kWh} \tag{6.11}$$

With this new perspective on the cost of the reserve, the cost per year becomes

$$\frac{\$0.00556}{kWh} \times 3.41 \frac{kWh}{day} \times 365 \frac{days}{yr} = \frac{\$6.91}{yr} \tag{6.12}$$

which is considerably lower than the benefit gained by reduced energy storage needs, which is also an upfront, fixed, investment cost.

6. Conclusion

Continued integration of renewable energy resources onto the electric grid increases variability and decreases grid stability. Energy storage can help mitigate some of these effects, but traditional energy storage, such as batteries, is typically expensive and has other disadvantages such as round trip inefficiency and limited lifetime. Real, high-speed solar panel data was used to characterize the stochastic energy output of PV sources, and the numerous challenges faced and methods used when manipulating this real-life data set were detailed. Two alternative methods were then presented to absorb or reduce the variability imposed upon the grid by PV or other generation.

Dynamic HVAC load compensation was proposed as a method to absorb or filter short-term PV variability and act as effective grid inertia that is being replaced by non-inertial generation. A proposed Butterworth filter power target technique balanced energy storage demands with decreased uncertainty. A small-scale model of a variable speed blower and fan was used to estimate filtering limitations imposed by undesirable acoustic effects and to provide a conversion between fan speed and power consumed. Physical ceiling and floor limitations as well as thermal limitations further constrain the available filtering potential. Considering all of the imposed limitations, the variation absorption or filtering capability of dynamic HVAC load compensation was analyzed for various building sizes and on-site solar penetrations. As would be expected, the larger the relative size of the HVAC power consumption to the PV power capacity, the greater the system ability to absorb variations in power production. Decreased limitations such as ramp rate and amplitude limits would also enable increased filtering capability. The reduction in battery storage capacity was briefly investigated and of note was the substantial reduction in energy that had to pass into and out of the battery when dynamic load compensation was implemented.

PV operating reserve curtailment was then introduced as a way to reduce variability both through cropping of power spikes through curtailment as well as partially compensating power “valleys” by utilizing PV operating reserve. The same Butterworth filter power target method was used for analysis, and the variability quantified in terms of absolute variation and integrated differences from the target set point. The idea of operating reserve curtailment then led to the argument that as prices of PV continue to come down, the cost of grid regulation should be included in the cost of installed PV and renewable resources just as it is for conventional grid generation. PV already can act as a grid resource rather than a grid nuisance by providing rapid response times to faults, frequency regulation, ramping capability, and other services. This mindset of solar as a grid resource makes operating reserve

curtailment an economical choice, and the cost comparison was provided for varying amounts of curtailment and PV price points. A proposed metric of optimality was presented that balances energy production with decreased variability. The results indicate that no one level of operating reserve curtailment is optimal for all days, and that depending upon the type of cloud cover experienced, the optimal energy-variability peak may lie beyond the economic break-even point and thus be cost constrained.

A proof-of-concept model for desired power point tracking or "DPPT" was demonstrated. The model was built up in stages, first implementing an MPPT incremental conductance algorithm, then replacing the converter with an average model and similar dynamics, then operating at a fixed fraction of the MPP, and finally tracking a dynamic Butterworth signal. The end result was an algorithm that could calculate and track a filtered version of the raw solar panel power available. By demonstrating that such operation can be accomplished with nothing more than a modified control scheme, there exists a clear path to real-life implementation in photovoltaic inverters without additional hardware. With the paradigm shift in PV variability mitigation requirements, implementing such a change will provide the necessary regulation for predictable power output at a lower cost than additional investment in chemical energy storage.

6.1. Future work

While the solar data used for this work was sufficient, rerunning simulations for an entire year or more of solar data would lead to more realistic results. Knowing now that 100 Hz effectively captures all meaningful dynamics, and taking lessons from the first PV acquisition, a repeat experiment could yield a continuous data set suitable for long-term analysis of variability mitigation techniques.

Regarding the HVAC analysis, full-scale data or experiments are essential to verify or adjust the assumptions made when investigating dynamic load compensation. With recent access to fan power and airflow measurements, data from full-scale HVAC units could be substituted in for the scaled approximations. Additionally, correlated audio recordings from actual labs or classrooms with power usage data could lead to better ramp rate and amplitude limit approximations. Occupancy sensor data is also available, so further analysis is encouraged to determine how much of the building is unoccupied at a given time and what additional flexibility that lends to HVAC power filtering. Along these same lines, water tank storage has a giant potential capacity for thermal energy absorption and little to no

limitation on ramp rate, so if such systems can be more accurately characterized, their thermal inertia could supplement that of buildings and air.

Much of this data could be gathered from sensors and fed to control algorithms, but public awareness would be excluded from such a setup. Future work should almost certainly include public education of the variability imposed on the grid by photovoltaic fluctuations and the mitigation techniques actively engaged in combatting it. The format could be as simple as an energy dashboard displaying prevented power variation and where that energy is being stored, diverted, or eliminated. After all, short-term variability of renewables is often overlooked, so if the problem is to be addressed, people first need to know that the problem exists and then need to know what solutions exist and how they work.

The DPPT algorithm still needs considerable optimization requirements before operational hardware may be realized. Of primary concern is the high-frequency oscillation in power output, which would be undesirable to connect to the grid. Additionally, future work will include investigating alternative set-point power targets. For example, short-term forecasts may be substituted for the Butterworth filter set points.

To summarize, both of the two proposed variability mitigation methods presented in this thesis are inexpensive alternatives to battery storage, needing little more than an advanced control to be implemented. However, each method is also incapable of removing all variability introduced by PV. Together (with other thermal storage outlets potentially utilized), the proposed alternatives can drastically decrease or eliminate necessary chemical energy storage, provide inexpensive grid stability resources, and enable increased penetration of renewable energy technologies for a clearer, brighter future.

References

[1] O. Ma, S. Capanna, F. Joseck, J. Nathwani, T. Nguyen, C. Richard, P. Spitsen, L. Boyd, C. Marcy, E. Doe, J. Davis, S. Esterly, D. Feldman, R. Fu, C. Johnson, E. Lantz, A. Livecchi, J. Logan, D. Mooney, R. Newmark, G. Porro, P. Schwabe, A. Smith, T. Tian, T. Williams, and K. Wipke, *2014 Renewable Energy Data Book*. Natl. Renew. Energy Lab., p. 3, 2014.

[2] S. Shivashankar, S. Mekhilef, H. Mokhlis, and M. Karimi, "Mitigating methods of power fluctuation of photovoltaic (PV) sources – A review," *Renew. Sustain. Energy Rev.*, vol. 59, pp. 1170–1184, Jun. 2016.

[3] IEEE Standards Coordinating Committee 21, *IEEE Guide for Design, Operation, and Integration of Distributed Resource Island Systems with Electric Power Systems*. 2011.

[4] R. A. Gansler, S. A. Klein, and W. A. Beckman, "Investigation of minute solar radiation data," *Sol. Energy*, vol. 55, no. 1, pp. 21–27, Jul. 1995.

[5] R. Perez, S. Kivalov, J. Schlemmer, K. Hemker, and T. Hoff, "Parameterization of site-specific short-term irradiance variability," *Sol. Energy*, vol. 85, no. 7, pp. 1343–1353, Jul. 2011.

[6] T. E. Hoff and R. Perez, "Quantifying PV power output variability," *Sol. Energy*, vol. 84, no. 10, pp. 1782–1793, Oct. 2010.

[7] Y. Yasaei, R. D. Robinett, and A. A. Mammoli, "Building ventilation system as a low-pass filter for intermittent photovoltaic electricity generation," in *2014 IEEE Conference on Technologies for Sustainability (SusTech)*, 2014, pp. 259–263.

[8] D. B. Crawley, L. K. Lawrie, F. C. Winkelmann, and C. O. Pedersen, "EnergyPlus: New capabilities in a whole-building energy simulation program," *Seventh Int. IBPSA Conf.*, pp. 51–58, 2001.

[9] F. Sehar, S. Rahman, and M. Pipattanasomporn, "Impacts of ice storage on electrical energy consumptions in office buildings," *Energy Build.*, vol. 51, pp. 255–262, Aug. 2012.

[10] S. W. Wang, "Use of phase change materials in buildings—Can they play a role in demand side management for smart grid?," *HVAC&R Res.*, vol. 17, pp. 615–618, 2011.

[11] Z. Xu, X. Guan, Q.-S. Jia, J. Wu, D. Wang, and S. Chen, "Performance analysis and comparison on energy storage devices for smart building energy management," *IEEE Trans. Smart Grid*, vol. 3, no. 4, pp. 2136–2147, Dec. 2012.

[12] C. J. C. Williams, J. O. Binder, and T. Kelm, "Demand side management through heat pumps, thermal storage and battery storage to increase local self-consumption and grid compatibility of PV systems," in *2012 3rd IEEE PES Innovative Smart Grid Technologies Europe (ISGT Europe)*, 2012.

[13] T. Zhou and W. Sun, "Optimization of battery & supercapacitor hybrid energy storage station in wind/solar generation system," *IEEE Trans. Sustain. Energy*, vol. 5, no. 2, pp. 408–415, Apr. 2014.

[14] G. Imre, M. Johnson, J. Vetrano, K. Lynn, W. Parks, R. Handa, L. Kannberg, S. Hearne, K. Waldrip, and R. Braccio, "Grid energy storage," *U.S. Department of Energy Grid Energy Storage Report*, 2013. [Online]. Available: http://www.sandia.gov/ess/docs/other/Grid_Energy_Storage_Dec_2013.pdf. [Accessed: 03-Oct-2016].

[15] X. Guan, Z. Xu, and Q.-S. Jia, "Energy-efficient buildings facilitated by microgrid," *IEEE Trans. Smart Grid*, vol. 1, no. 3, pp. 243–252, Dec. 2010.

[16] Z. Wang, R. Yang, and L. Wang, "Multi-agent control system with intelligent optimization for smart and energy-efficient buildings," in *IECON 2010 - 36th Annual Conference on IEEE Industrial Electronics Society*, 2010, pp. 1144–1149.

[17] T. Wei, T. Kim, S. Park, Q. Zhu, S. X.-D. Tan, N. Chang, S. Ula, and M. Maasoumy, "Battery management and application for energy-efficient buildings," in *Proceedings of the 51st Annual Design Automation Conference - DAC '14*, 2014.

[18] E. Saberbari and H. Saboori, "Net-zero energy building implementation through a grid-connected home energy management system," in *2014 19th Conference on Electrical Power Distribution Networks (EPDC)*, 2014, pp. 35–41.

[19] "Apple campus approved by cupertino council," *Sky News*, 2013. [Online]. Available: http://news.sky.com/story/1155428/apple-campus-approved-by-cupertino-council. [Accessed: 15-Jul-2015].

[20] H. Hao, T. Middelkoop, P. Barooah, and S. Meyn, "How demand response from commercial buildings will provide the regulation needs of the grid," in *2012 50th Annual Allerton Conference on Communication, Control, and Computing (Allerton)*, 2012, pp. 1908–1913.

[21] S. Meyn, "Value and cost of renewable energy: distributed energy management," presented at *The Joint JST-NSF-DFG Workshop*, Honolulu, USA, 2014.

[22] J. Glover and F. Schweppe, "Advanced load frequency control," *IEEE Trans. Power Appar. Syst.*, vol. PAS-91, no. 5, pp. 2095–2103, Sep. 1972.

[23] Y. Ma, A. Kelman, A. Daly, and F. Borrelli, "Predictive control for energy efficient buildings with thermal storage: modeling, simulation, and experiments," *IEEE Control Syst.*, vol. 32, no. 1, pp. 44–64, Feb. 2012.

[24] C. Szasz, "HVAC elements modeling and implementation for net-zero energy building applications," in *2014 IEEE 9th IEEE International Symposium on Applied Computational Intelligence and Informatics (SACI)*, 2014, pp. 195–200.

[25] P. Hernandez and P. Kenny, "From net energy to zero energy buildings: Defining life cycle zero energy buildings (LC-ZEB)," *Energy Build.*, vol. 42, no. 6, pp. 815–821, Jun. 2010.

[26] L. Pérez-Lombard, J. Ortiz, and C. Pout, "A review on buildings energy consumption information," *Energy Build.*, vol. 40, no. 3, pp. 394–398, Jan. 2008.

[27] M. Maasoumy, B. M. Sanandaji, A. Sangiovanni-Vincentelli, and K. Poolla, "Model predictive control of regulation services from commercial buildings to the smart grid," in *2014 American Control Conference*, 2014, pp. 2226–2233.

[28] N. Etherden and M. H. J. Bollen, "Increasing the hosting capacity of distribution networks by curtailment of renewable energy resources," in *2011 IEEE Trondheim PowerTech*, 2011.

[29] Y. Dvorkin, M. A. Ortega-Vazquez, and D. S. Kirschen, "Wind generation as a reserve provider," *IET Gener. Transm. Distrib.*, vol. 9, no. 8, pp. 779–787, 2015.

[30] R. Tonkoski, L. A. C. Lopes, and T. H. M. El-Fouly, "Coordinated active power curtailment of grid connected PV inverters for overvoltage prevention," *IEEE Trans. Sustain. Energy*, vol. 2, no. 2, pp. 139–147, 2011.

[31] R. J. Serna, B. J. Pierquet, J. Santiago, and R. C. N. Pilawa-Podgurski, "Field measurements of transient effects in photovoltaic panels and its importance in the design of maximum power point trackers," in *Conference Proceedings - IEEE Applied Power Electronics Conference and Exposition - APEC*, 2013, pp. 3005–3010.

[32] J. A. Magerko, Y. Cao, and P. T. Krein, "Quantifying photovoltaic fluctuation with 5 kHz data: Implications for energy loss via maximum power point trackers," in *2016 IEEE Power and Energy Conference at Illinois (PECI)*, 2016.

[33] "Canada Goose information, photos, and facts," *American Expedition!*, 2015. [Online]. Available: https://forum.americanexpedition.us/canada-goose-information-facts-photos-and-artwork. [Accessed: 07-Sep-2016].

[34] M. Ogilvie and S. Young, *Wildfowl of the World*. New Holland Publishers, 2004.

[35] Y. Cao, J. A. Magerko, T. Navidi, and P. T. Krein, "Dynamic filtering of stochastic solar resources using HVAC drive control – A determination of feasible bandwidth," in *2015 IEEE Energy Conversion Congress and Exposition (ECCE)*, 2015, pp. 3127–3134.

[36] Y. Cao, J. A. Magerko, T. Navidi, and P. T. Krein, "Dynamic energy management needs in low-energy buildings imposed by stochastic solar resources," in *2015 International Conference on Complex Systems Engineering (ICCSE)*, 2015.

[37] K. Kedzior and S. Knight, "Electrical and Computer Engineering Building opens at the University of Illinois at Urbana-Champaign," *SmithGroup JJR News Release*, 2014. [Online]. Available: http://www.smithgroupjjr.com/news_releases/electrical-and-computer-engineering-building-opens-at-the-university-of-illinois-at-urbana-champaign. [Accessed: 07-Apr-2016].

[38] A. Lopez, B. Roberts, D. Heimiller, N. Blair, and G. Porro, "U.S. renewable energy technical potentials: a GIS-based analysis," Golden, CO, 2012.

[39] Y. Cao, J. A. Magerko III, T. Navidi, and P. T. Krein, "Power electronics implementation of dynamic thermal inertia to offset stochastic solar resources in low-energy buildings," *Proc. J. Emerg. Sel. Top. Power Electron.*, 2016.

[40] J. A. Magerko and P. T. Krein, "Opportunities for photovoltaic system operation below parity: Costs and benefits of active grid support," in *In Proc. 2016 IEEE Photovoltaic Specialists Conference (PVSC)*, 2016.

[41] A. Safdarian, M. Fotuhi-Firuzabad, and F. Aminifar, "Compromising wind and solar energies from the power system adequacy viewpoint," *IEEE Trans. Power Syst.*, vol. 27, no. 4, pp. 2368–2376, Nov. 2012.

[42] M. Hummon, P. Denholm, J. Jorgenson, D. Palchak, B. Kirby, and P. Ma, "Fundamental drivers of cost and price of operating reserves," 2013.

[43] R. Bründlinger, "Advanced smart inverter and DER functions requirements in latest European Grid Codes and future trends," in *Smart Inverters and System Benefits Breakout Session at the Solar Canada 2015 Conf.*, 2015.

[44] P. T. Krein and R. S. Balog, "Cost-effective hundred-year life for single-phase inverters and rectifiers in solar and LED lighting applications based on minimum capacitance requirements and a ripple power port," in *2009 Twenty-Fourth Annual IEEE Applied Power Electronics Conference and Exposition*, 2009, pp. 620–625.

[45] T. Esram, P. T. Krein, B. T. Kuhn, R. S. Balog, and P. L. Chapman, "Power electronics needs for achieving grid-parity solar energy costs," in *2008 IEEE Energy 2030 Conference*, November 2008.

[46] "Grid-tied systems with SolarEdge power optimizers," *Wholesale Solar*. [Online]. Available: http://www.wholesalesolar.com/free-racking-sale. [Accessed: 22-Jan-2016].

[47] H. K. Trabish, "Utility-scale solar booms as costs drop, challenging gas on price," *Utility Dive Newsletter*, 2015.

[48] "Tesla Powerwall overview," *Wholesale Solar*, 2016. [Online]. Available: http://www.wholesalesolar.com/tesla-powerwall-for-solar. [Accessed: 16-May-2016].

[49] "Tesla Motors (TSLA) earnings report: Q1 2015 conference call transcript," 2015. [Online]. Available: https://www.thestreet.com/story/13142191/4/tesla-motors-tsla-earnings-report-q1-2015-conference-call-transcript.html. [Accessed: 16-May-2016].

[50] "Average retail price of electricity, monthly," *Electricity Data Browser. U.S. Energy Information Administration*, 2016. [Online]. Available: http://www.eia.gov/electricity/data/browser/. [Accessed: 16-May-2016].